Cell Reports
Physical Science

CellPress
OPEN ACCESS

Article

Salt-rejecting continuous passive solar thermal desalination via convective flow and thin-film condensation

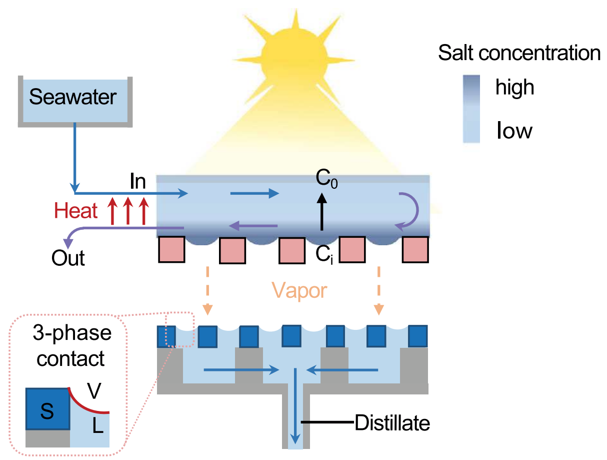

Patrick I. Babb, S. Farzad Ahmadi, Forrest Brent, ..., Tyler Susko, Kirk Fields, Yangying Zhu

yangying@ucsb.edu

Highlights

Passive inverted single-stage solar desalinator achieves continuous desalination

Salt rejection by diffusion for 7 days

Efficient thin-film condensation on hydrophilic microstructures

Transport model to guide further optimization

Developing passive systems to convert seawater to fresh water is of great importance. Babb et al. develop a passive inverted single-stage solar desalinator under one-sun illumination, which utilizes thin-film evaporation and condensation. This method achieves high-performance continuous desalination for 7 days.

Babb et al., Cell Reports Physical Science 4, 101682
December 20, 2023 © 2023
https://doi.org/10.1016/j.xcrp.2023.101682

Cell Reports
Physical Science

Article

Salt-rejecting continuous passive solar thermal desalination via convective flow and thin-film condensation

Patrick I. Babb,[1,4] S. Farzad Ahmadi,[1,2,4] Forrest Brent,[1] Ruby Gans,[1] Mabel Aceves Lopez,[1] Jiuxu Song,[1] Qixian Wang,[1] Brandon Zou,[1] Xiangying Zuo,[1] Amanda Strom,[3] Jaya Nolt,[3] Tyler Susko,[1] Kirk Fields,[1] and Yangying Zhu[1,5,*]

SUMMARY

Passive solar desalination is an emerging low-cost technology for freshwater production. State-of-the-art desalinators typically evaporate water using wicking structures to achieve high solar-to-vapor efficiency. However, wicking structures have limited salt rejection capability, which typically limits the operating duration to several hours. In addition, few studies have demonstrated efficient condensation to achieve a high solar-to-water efficiency. Here, we report a passive inverted single-stage solar desalinator that achieves continuous desalination and efficient condensation by convection-mediated salt diffusion and a novel mode of thin-film condensation. We experimentally demonstrate a record-high continuous passive desalination and salt rejection test duration of 168 h (7 days) under one-sun illumination. Our desalinator achieves a water collection rate of 0.5 kg m^{-2} h^{-1}, which corresponds to a 32.9% solar-to-water efficiency. Furthermore, we develop a theoretical transport model and perform a parametric study to guide further optimization. This work signifies an improvement in the robustness of current state-of-the-art desalinators.

INTRODUCTION

Water and energy are among the greatest challenges of the 21st century, yet current industrial-scale desalination technologies including reverse osmosis and distillation are still energy-intensive.[1,2] Solar thermal desalination is an attractive passive technology where sunlight is utilized as heat to vaporize water,[3] which can then be condensed to pure liquid water. These devices are potentially cost-effective and portable, making them suitable for developing countries where water scarcity is most severe.[4] So far, most previous works have focused on engineering solar-absorbing porous materials to localize solar heat to the liquid-vapor interface.[5–14] Highly efficient evaporation can be achieved by avoiding heating the bulk of water and minimizing conduction, convection, and radiation heat loss. Solar-to-vapor efficiency, usually defined as the total latent energy required to produce a certain mass of vapor over the input sunlight,[15] exceeding 90% has been demonstrated under concentrated and one sun conditions.[11]

Despite the advancements in evaporator development, only a few recent works have incorporated condensation, which is a necessary step to convert water vapor back to liquid water, into their desalination systems.[16–22] Most of these full systems have an

---

[1] Mechanical Engineering Department, University of California, Santa Barbara, Santa Barbara, CA 93106, USA

[2] Department of Physics and Engineering, McDaniel College, Westminster, MD 21157, USA

[3] Materials Research Laboratory, University of California, Santa Barbara, Santa Barbara, CA 93106, USA

[4] These authors contributed equally

[5] Lead contact

*Correspondence: yangying@ucsb.edu

https://doi.org/10.1016/j.xcrp.2023.101682

inverted design, where the condenser is below the evaporator to avoid blocking the sunlight. To reduce the thickness of liquid in the evaporator, several inverted systems employed a thin wicking layer to feed salt water using capillarity to the solar absorber for evaporation. The minimum amount of water in the wicking layer significantly reduced heat loss. As such, solar-to-water efficiency as high as 70% has been demonstrated under one sun for single-stage devices,[16] and even higher solar-to-water efficiencies are achieved with multi-stage devices.[17,21,23,24] Solar-to-water efficiency is evaluated using the mass of collected liquid water as opposed to the mass of the evaporated water vapor in the solar-to-vapor efficiency. However, the wicking design lacks a mechanism to discharge salt out of the desalination device over prolonged operation; therefore, the high efficiencies are mainly demonstrated with pure water. With salt water, salt crystals were observed on the evaporator as soon as 2 h after being exposed to sunlight.[18] Several recent salt-rejecting designs utilized a contactless absorber,[9] salt diffusion,[9,18,25] and Marangoni flow,[26] yet most of these systems only have the evaporator with no condenser. A full system with a sustained salt rejection mechanism that allows continuous desalination without efficiency decay is highly desirable.

Furthermore, most previous work incorporated dropwise condensation on hydrophobic surfaces. While dropwise condensation has a higher heat transfer coefficient than the conventional filmwise condensation, it relies on a hydrophobic coating, which has been known to suffer from durability issues.[27,28] Dropwise condensation also relies on gravity to remove the condensed drops and therefore cannot be positioned horizontally. In fact, several previous studies reported droplets stuck to the condenser surface which reduced the amount of collected liquid.[17,18] In addition, efficient vapor transport from the evaporator to the condenser is also critical to ensure a high solar-to-water efficiency. This requires a minimal gap distance between the evaporator and the condenser surface, assuming that there is sufficient thermal isolation between the evaporator and the condenser. This is difficult to achieve with condenser surfaces that are not parallel to the evaporator. Several works use nanophotonics-enhanced solar membrane distillation (NESMD), where a single hydrophobic membrane is used for heat localization on one side and membrane distillation on the other side.[19,29,30] Many NESMD works promote vapor transport by ensuring that the distance between the evaporation and condensation interfaces is the thickness of the membrane and utilizes convection to reject salt. However, it is difficult to minimize heat loss from the evaporation interface to the condensation interface, which motivates some works to employ more complex sweeping gas membrane distillation.[29,31] Thermally isolating the evaporation and condensation surfaces is desired to maintain a high temperature difference and a high efficiency.

Here, we designed a full system with the following key considerations as shown in Figure 1. On the evaporator side, salt water flows from a reservoir into the evaporator driven by gravity. A thin liquid layer is maintained on the top of a hydrophobic, solar-absorbing membrane. Sunlight is absorbed as heat on the membrane, which evaporates water. Evaporation increases the local concentration of salt, which diffuses back to the bulk flow. The higher-salinity water is discharged from the evaporator. This discharge mechanism allows the amount of salt within the evaporator to reach equilibrium over time, as opposed to continuously increasing in a wick structure. This allows continuous desalination without salt precipitation. To reduce sensible heat loss associated with the discharged water, we recycle the heat of the discharged water to preheat the incoming water by designing a counter-flow heat exchanger (Figures 1A and 1B).

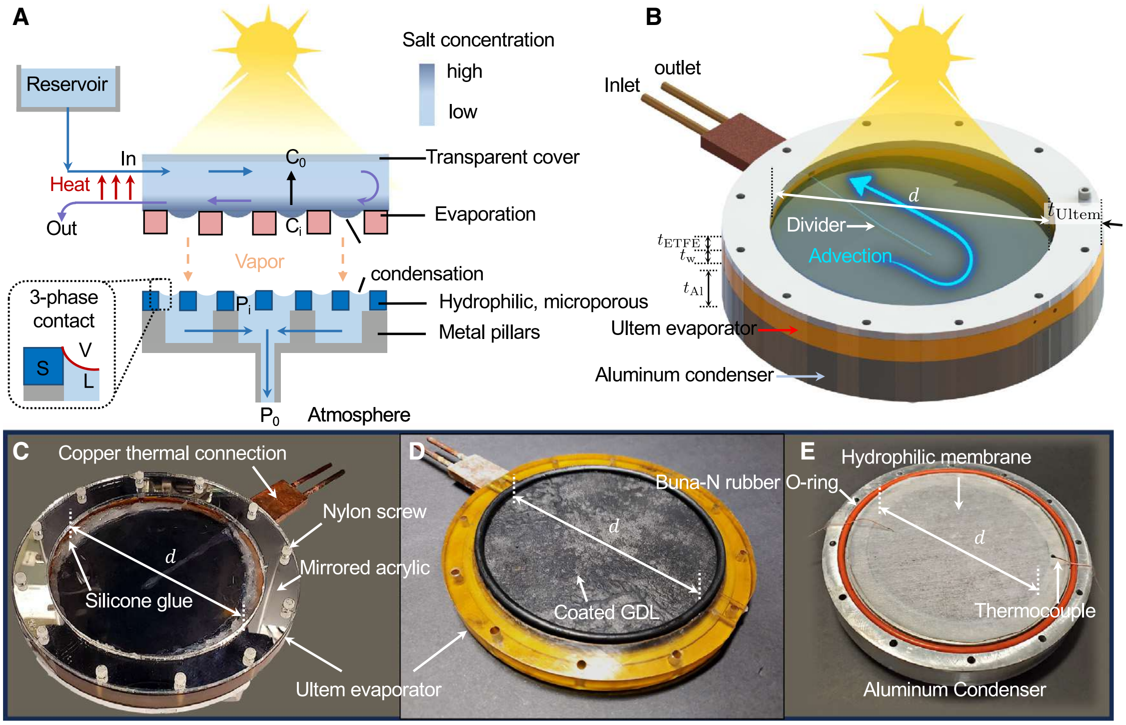

Figure 1. Design of the salt-rejecting desalination concept

(A) Cross-section drawing of the desalination design and transport mechanisms.

(B) Schematic shows the passive salt-rejecting desalination device is composed of an Ultem evaporator and an aluminum condenser. The path of the fluid flow is indicated by a blue arrow, wherein the water enters through the inlet and travels over the evaporator, and finally exits through the outlet. In addition, an efficient thermal connection is established through copper, allowing the warm water leaving the outlet to preheat the cool water entering the inlet, further optimizing the desalination process. (C–E) Present optical images of the device, providing visual representations of its components and structure.

(C) The assembled device, featuring the evaporator and condenser elements, along with mirrored acrylic and ETFE film.

(D) A bottom view of the evaporator, which supports the gas diffusion layer (GDL) covered with black carbon nanoparticles.

(E) A top view of the condenser with a white hydrophilic membrane on top. See Figure S12 for the comprehensive dimensions of the device.

On the condenser side, we designed a microporous membrane for highly efficient thin-film condensation as shown in Figure 1A. Different from conventional dropwise and filmwise condensation on a solid surface where droplets condense and shed on the same side of the surface, the vapor condenses on the front side of the membrane and the condensed liquid is collected from the backside. This way, the condenser membrane can theoretically be placed extremely close to the evaporator membrane, allowing minimal vapor transport resistance. Analogous to thin-film evaporation from micro/nanostructures, which achieves the highest phase change heat transfer coefficient, thin-film condensation in microporous membrane allows abundant three-phase contact region (Figure 1A) and can therefore potentially achieve a higher condensation heat transfer coefficient compared with dropwise condensation, if designed properly.[32–34] Furthermore, the condenser membrane is hydrophilic and capillary pressure was utilized to lower the local liquid pressure within the pores. This promotes the condensed liquid to spontaneously enter the backside of the membrane, which prevents flooding of liquid on top of the membrane. This low pressure is created simply via a hydrostatic pressure between the membrane and the outlet of the condensed liquid, which is at atmospheric pressure. A schematic of the device that we developed is illustrated in Figure 1B, and images of the assembled device, a bottom-up view of the evaporator, and a top-down view of the condenser are shown in Figures 1C–1E, respectively. Different from

NESMD, which rejects condensation heat to the cold liquid flow, the heat in our system is rejected directly to the much higher thermal conductivity solid substrate at the three-phase contact, which then is rejected to the ambient through the condenser surface. Therefore, a flowing liquid is not required and the condensate simply drains to be collected.

The passive, single-stage device achieves continuous seawater desalination under one sun for 1 week (168 h) without any efficiency decay, signifying insignificant salt accumulation on the evaporator. To the best of our knowledge, this work demonstrates the longest passive continuous salt water to fresh water distillate production to date compared with state-of-the-art solar thermal desalinators.[10,16–18,21,24] The maximum solar-to-water efficiency measured on seawater is 32.9%, which agrees with a theoretical model that we developed. The model proposes that enhancing the thermal insulation of the upper transparent cover and optimizing its transmittance, enhancing the effective heat transfer coefficient between the condenser and the ambient air, as well as improving the absorptance of the evaporator membrane, can lead to a further increase in efficiency, achieving a value as high as 90%.

RESULTS

Design and characterization of a solar-powered desalinator

The desalinator consists of three primary components: the reservoir, the evaporator, and the condenser, as shown in Figure 1A. Liquid flows from the reservoir into the evaporator driven by gravity. An ethylene tetrafluoroethylene (ETFE) transparent cover transmits sunlight to a microporous solar-absorbing and hydrophobic evaporator membrane. Salt water is sandwiched between the ETFE transparent cover and the evaporator membrane. The evaporator membrane was fabricated by coating carbon black nanoparticles onto a commercially available gas diffusion layer (GDL) using polydimethylsiloxane (PDMS) with curing agent as the binder (Figures 1D, 2A, and 2B). The GDL is a fibrous, Teflon-treated carbon paper with a porosity of 78%.[35] Two copper tubes serve as the water inlet and outlet of the evaporator to maintain a salt concentration in the evaporator chamber below saturation. The copper tubes are thermally connected so that exiting warm water preheats the incoming cool water to recover thermal energy. Above the evaporator there is a polyethylene terephthalate glycol (PETG) divider to separate the inlet from the outlet such that liquid will flow across the entire evaporator membrane before being discharged (Figure 1B).

The evaporator and condenser are separated by a thin air gap (t_a = 3 mm, using a rubber O-ring) that allows efficient vapor transport from the evaporator to the condenser while still maintaining a temperature difference or thermal isolation. A thinner gap distance reduces the vapor transport resistance, which is modeled using Fick's law but may increase the heat conduction across the air gap between the evaporator to the condenser. In addition, as the temperature of the water above the evaporator increases, the solubility of air in the water decreases, which can cause air bubbles to form on the evaporator membrane. To mitigate this problem, a small opening is introduced on the O-ring to allow air to vent. The condenser membrane is a hydrophilic microporous paper (pore size approximately 100–580 μm) made of 55% cellulose and 45% polyester (Figures 2C and S2A, Texwipe TX609),[36] which provides ample three-phase contact area for effective condensation. To reject heat, the microporous paper is supported by thermally conductive metal structures on an aluminum plate, where heat is dissipated to the environment through natural air convection. Two configurations were investigated. We machined grooves directly on

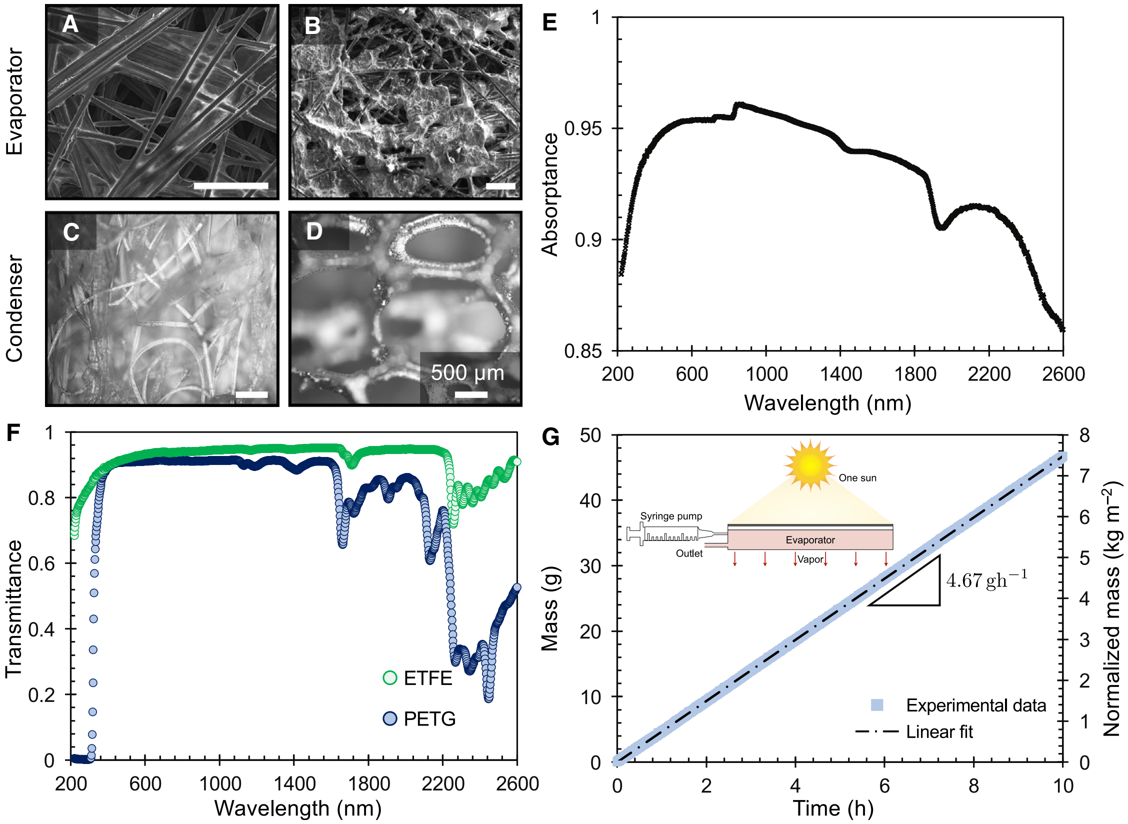

Figure 2. Characterization of optical properties and vapor production of the evaporator

(A) Scanning electron microscopy (SEM) image of the GDL substrate alone.

(B) SEM image of the evaporator membrane composed of the GDL substrate coated with PDMS and carbon black nanoparticles.

(C) Optical image of the microporous paper condenser membrane.

(D) Optical image of the nickel foam.

(E) Absorptivity of the evaporator membrane using the UV-Vis-NIR spectrophotometer.

(F) Transmittance spectra of the ETFE and PETG films used as a transparent cover and divider, respectively.

(G) Vapor production from the evaporator membrane is 4.67 g h^{-1} corresponding to 0.73 kg m^{-2} h^{-1}. The inset figure illustrates the evaporator used without the condenser to measure the vapor flux. Experiments in (G) were conducted in a room with an average temperature and relative humidity of 20°C and 54%, respectively.

the aluminum plate (v1-condenser, Figure S2G), and also placed a porous nickel foam (Figures 2D and S2B) on a flat aluminum plate (v2-condenser, Figure S2). The grooves and the large pores of the nickel foam (Figure 2D) allow the condensed fresh water to flow laterally with a low viscous resistance to an outlet positioned at the center of the device (Figures 1A and S1; Note S1). The v1-condenser eliminates a contact resistance between the nickel and the aluminum but requires machining. The nickel foam (v2-condenser) offers a simple alternative approach. As we show later, the two condensers performed similarly.

We characterized the optical property of the membranes and films through ultraviolet-visible-near-infrared (UV-Vis-NIR) spectrophotometry. Figure 2E shows that the evaporator membrane has an absorptivity, α_{evap} greater than 0.9 for the majority of the solar spectrum between 200 nm and 2.6 μm and an absorptivity greater than 0.85 for the solar spectrum between 200 nm and 2.6 μm. This result shows that the evaporator membrane is absorbing the vast majority of incoming solar light and heating since about 99% of solar radiation is contained in the region between 300 nm and 3 μm.[37] Figure 2F illustrates that ETFE, the transparent cover for the device, has a transmittance τ_{ETFE} of greater than 0.9 for the majority of the spectrum between 200 nm and 2.6 μm, which allows for high solar transmission to the membrane. Since the layer of water sandwiched between the evaporator and ETFE is thin (~1 mm), we estimate that less than 80% of the incoming solar energy ($\tau_{\mathrm{ETFE}} \times \alpha_{\mathrm{evap}}$) is used to heat the evaporator membrane. The thickness of water increases to 5 mm at the inlet and outlet to allow water from the copper tubes to enter the desalinator freely. The divider has a lower transmittance than ETFE, which declines after 1.5 μm; however, the divider is only exposed to a negligibly small portion of the evaporator membrane.

Experimental results

In this section, three test regimes were conducted: an evaporator-only test characterizing the solar-to-vapor efficiency, a passive full system test lasting 7 days using a gravity feed bag (2 trials), and a full system test lasting 7 days using active pumping as a control experiment. For all three tests, we used salt water obtained from Goleta Beach in California. The salinity is 3.15%, measured using an ORAPXI digital salinity tester (SL-A100). All the tests were conducted under a solar simulator (Newport ORIEL SOL3A) with continuous solar flux of 1,000 W m^{-2} (one sun). The diameter of the exposed evaporator membrane is 9 cm, which corresponds to an area of $A_0 \approx 0.0064\ \mathrm{m}^2$.

Before characterizing the full system, the liquid-to-vapor efficiency of the evaporator was first tested for 10 h. The device has only the evaporator that evaporates water into ambient air (inset, Figure 2G). To estimate an upper limit of the solar-to-vapor efficiency corresponding to a minimal liquid flow rate, we used a syringe pump to supply salt water to the evaporator and gradually reduced the flow rate until the flow rate of the discharged water was negligibly low. At this condition, the inlet flow rate was 4.9 mL h^{-1} and the discharged flow rate was measured to be 0.18 mL h^{-1}. The mass of the evaporated liquid over time shown in Figure 2G was calculated by subtracting the mass of the discharged water measured using a mass balance from the mass of the supplied liquid. Although this discharge flow rate may be too low to avoid salt precipitation on the evaporator membrane over an extended period of time, the salinity of seawater on the evaporator after the 10-h test concluded was 3.32 wt %, well below the saturation concentration of 26.89 wt %. This saturation concentration is evaluated at 50°C, which was roughly the evaporator temperature.[38] No salt precipitation was observed on the evaporator membrane immediately after the experiment.

As seen in Figure 2G, the evaporator membrane alone has a vapor production rate of 4.67 g h^{-1} or 0.73 kg $\mathrm{m}^{-2}\ \mathrm{h}^{-1}$ corresponding to a solar-to-vapor efficiency of 49.1%. The definition of efficiency is

$$\eta = \frac{\dot{m}\, h_{\mathrm{fg}}}{q_{\mathrm{solar}} A_0} \qquad \text{(Equation 1)}$$

where $\dot{m}$ is the mass flow rate, $h_{\mathrm{fg}} = 2381.9\ \mathrm{kJ\ kg}^{-1}$ is the latent heat of vaporization at 50°C. We chose the latent heat at 50°C, because this is the approximate evaporator temperature we observed in subsequent experiments using the same evaporator membrane and ETFE transparent film. Only latent heat, not sensible heat, is considered in the solar-to-vapor efficiency result. The evaporator efficiency could be improved by improving thermal insulation of the top transparent cover, as suggested in our model in a later section. Natural convection in the liquid layer will also lead to heat loss from the membrane to the bulk liquid. This could be suppressed by improving the heat-recycling design at the inlet and outlet. Many recent

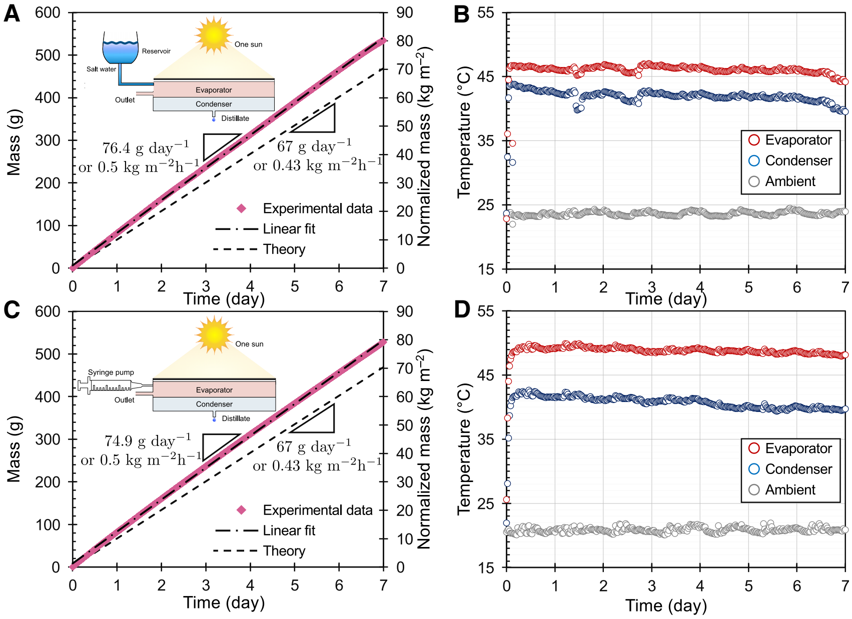

Figure 3. Comprehensive 7-day performance analysis of the device utilizing saline seawater and solar flux of 1,000 W m $^{-2}$

The assessment encompassed two distinct approaches, namely, fully passive gravity-driven water container testing (A and B) and controlled flow rate via a syringe pump (C and D).

(A) Inlet seawater salinity recorded at 3.15 wt %. The average inlet flow rate over the duration of the test was 7 g h $^{-1}$.

(B) During the full passive gravity-driven water container testing, the experiment entailed continuous monitoring of the mass rate (pink data points in A) and corresponding temperatures of the ambient, condenser, and evaporator (B). The fully passive experiment was conducted in a laboratory setting with an average temperature of $T_{amb} \approx 23$ºC and a relative humidity of RH ≈ 54%.

(C) The experiment involved a saltwater inlet flow rate of 5 mL h^{-1}.

(D) During the experiment, the corresponding temperatures of the ambient, condenser, and evaporator were observed and recorded. The experiment was conducted in a laboratory setting with an average temperature of $T_{amb} \approx$ 21°C and relative humidity of RH ≈ 60%. The results of the experiment are compared with the theoretical model, represented by the black dashed line in (A) and (C). In addition, a linear fit to the experimental data points is shown as the black dotted line in (A) and (C). The laboratory test setups are depicted schematically in insets in (A) and (C).

works on the evaporator without the condenser reported solar-to-vapor efficiency above 85%.[7,39–47] The high efficiency was typically achieved by positioning a membrane on top of the liquid, so the natural convection in the liquid is suppressed, effectively localizing heat to the membrane. However, such a design if made into a full system would require a condenser on top of the evaporator, which is impractical as the condenser will block sunlight.

Subsequently, a comprehensive system encompassing both the evaporator and the v1-condenser was assembled, and two protracted passive desalination tests were carried out, extending over a duration of 7 days. Figure S3 and the inset of Figure 3A illustrate the test setup. Salt water flows from a reservoir made of a water bottle to the desalinator driven by gravity. The distillate production as a function of time was measured by a mass balance (see experimental procedures). We determined the flow rate from the gravity feeding bag by determining the distillate rate and outlet flow rate from the distillate mass balance and outlet mass balance. For the first passive desalination test, the average flow rate over the duration of the test was 7 g h^{-1} (Figure S4). Figure 3A illustrates the distillate production as a function of time.

The rate of fresh water collection does not decay even after 7 days (168 h) of continuous operation under one sun illumination, which indicates that the pore sizes of the evaporator membrane possibly remained unchanged and we further hypothesize that no salt crystals were formed. As seen in Figure 3A, we achieved a distillate production rate of 76.4 g day^{-1}, which corresponds to 0.497 kg m^{-2} h^{-1} over 7 days in one sun using the passive method and a 32.9% solar-to-water efficiency. The experimental efficiency is in line with our model where we obtained a 0.43 kg m^{-2} h^{-1} production rate corresponding to a 28.9% efficiency. Note S2 describes the model used to obtain this efficiency. The temperatures of the evaporator and the condenser membranes are shown in Figure 3B. Throughout the duration of the 7-day experiment, the mean temperatures for the condenser, evaporator, and ambient environment were ascertained to be, $T_c \approx 42^\circ C$, $T_e \approx 46^\circ C$, and $T_{amb} \approx 23^\circ C$, respectively. For the second passive desalination test (Figure S5), the average flow rate over the duration of the test was 7.2 g h^{-1} (Figure S6). We achieved a distillate production rate of 71.3 g day^{-1}, which corresponds to 0.47 kg m^{-2} h^{-1} over 7 days in one sun using the passive method and a 30.7% efficiency. We attribute the experimental efficiency difference to varying environmental conditions. Throughout the duration of the second 7-day experiment, the mean temperatures for the condenser, evaporator, and ambient environment were ascertained to be, $T_c \approx 41^\circ C$, $T_e \approx 43^\circ C$, and $T_{amb} \approx 24^\circ C$, respectively. Between the two passive 7-day desalination tests we achieved a distillate salinity as low as 0.00 wt %. In addition, we performed inductively coupled plasma analysis on the distillate and found that the ion concentrations in the distillate were below the WHO health guideline and taste threshold as well. The ion concentrations from the desalinator are listed in Note S4 and Table S2.

Furthermore, an additional 7-day desalination experiment was conducted, wherein a syringe pump was utilized to ensure a consistent flow rate of 5 mL h^{-1}, serving as a control experiment. The full system consists of the evaporator and the v2-condenser (Figure S2) and the experimental setup is shown in Figure S7. The flow rate of 5 mL h^{-1} was determined to be sufficient in avoiding salt precipitation as the concentration of discharged salt water from the outlet was 5.60 wt % after 7 days, which was lower than the saturation salt concentration of 26.889 wt %. Figure 3C illustrates the distillate production as a function of time. We achieved a distillate production rate of 74.9 g day^{-1} or 0.487 kg m^{-2} h^{-1} which corresponds to an efficiency of 32.0%. This efficiency is similar to the efficiency of the 7-day passive test, which suggests that the efficiency is relatively insensitive to changes in the flow rate for the conditions that we tested. The measured salinity of the distillate was also 0.00 wt %. Figure 3D demonstrates temperatures of the evaporator membrane, condenser membrane as well as the ambient temperature of the laboratory during the 7-day experiment. Throughout the duration of the 7-day experiment, the mean temperatures for the condenser, evaporator, and ambient environment were ascertained to be $T_c \approx 41^\circ C$, $T_e \approx 49^\circ C$, and $T_{amb} \approx 21\ ^\circ C$, respectively.

Heat and mass transfer model

In this section, we introduce a comprehensive heat and mass transport model to gain insights into both the solar-to-water efficiency and the energy loss mechanisms within our system. We first present the model framework and validate it through passive experimental results. Subsequently, we explore the impact of varying design parameters on system efficiency.

Model framework

Figures 4A and 4B show an equivalent thermal resistance network and the energy flow of the system, respectively. Consider the heat and mass transfer at steady-state

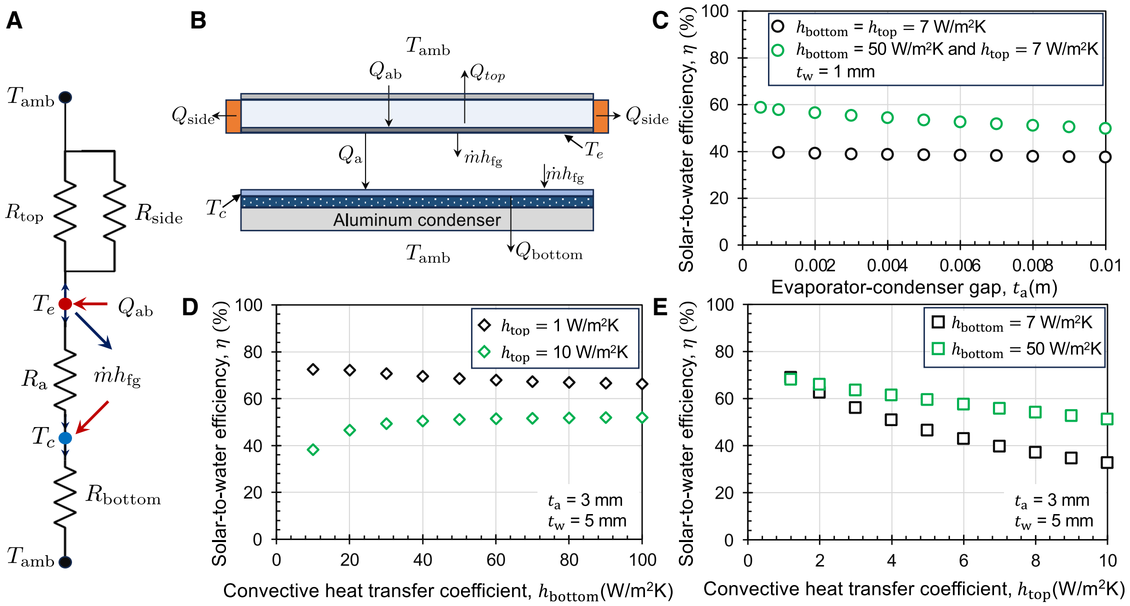

Figure 4. Energy flow to unveil the theoretical solar-to-water efficiency

(A) The equivalent thermal resistance network.

(B) Schematic of the cross-section of the device and energy flow. For a scaled-up device, we exclude Q_{side} from our calculations because, Q_{side} is negligibly small.

(C) The relationship between solar-to-water efficiency and the gap between the evaporator and condenser (D) and natural heat transfer coefficient on top of the ETFE film (E) and the natural heat transfer coefficient on the bottom of the aluminum surface is examined by solving Equations 2, 3, and 4 with an assumed ambient temperature of 20°C.

conditions, the evaporator absorbs heat from the sunlight $Q_{ab} = \tau_f \alpha_a q_{solar} A_0$, where τ_f is the transmittance of the ETFE film, and α_a is the absorptance of the evaporator membrane, and absorber area A_0. Evaporation occurs on the membrane, which removes heat $\dot{m}h_{fg}$ from the evaporator membrane, where $\dot{m}$ is the mass flow rate of vapor production (kg/s) and h_{fg} is the latent heat of vaporization. The evaporator loses heat through the top surface Q_{top}, through the side Ultem Q_{side}, and through the air gap to the condenser Q_{air}. The sensible heat loss from the discharged salt water is neglected by assuming effective heat recycling due to the counter-flow heat exchanger. Heat conduction through the O-ring from the evaporator to the condenser is neglected due to its minimal contact area with the membranes. The vapor condenses on the condenser membrane, which releases the same amount of latent heat $\dot{m}h_{fg}$ on the condenser membrane. The condenser membrane also receives heat from the evaporator through heat conduction across the air gap Q_{air}, and rejects heat to the ambient via the aluminum Q_{bottom}.

In the equivalent thermal resistance network, balancing the heat gain and heat loss at the evaporator membrane (T_e) and condenser membrane (T_c) requires

$$Q_{ab} - \frac{T_e - T_{amb}}{R_{top}} - \frac{T_e - T_{amb}}{R_{side}} - \frac{T_e - T_c}{R_a} - \dot{m}h_{fg} = 0, \qquad \text{(Equation 2)}$$

$$\dot{m}h_{fg} + \frac{T_e - T_c}{R_a} - \frac{T_c - T_{amb}}{R_{bottom}} = 0. \qquad \text{(Equation 3)}$$

In Equations 2 and 3, T_e, T_c, and T_{amb} are temperatures of the evaporation interface (or the evaporator membrane), the condensation interface (or the condenser membrane), and the ambient. R_{top}, R_{side}, R_a, and R_{bottom} are the total thermal resistances and defined as $R = \Delta T / Q$ for Q_{top}, Q_{side}, Q_{air}, and Q_{bottom}, detailed in Note S2 and Figure S11. The thermal resistances are only functions of the geometry and the thermal conductivity of the materials in the device, and the air convection heat transfer coefficient on the external surface of the device. Furthermore, vapor transport between the evaporator and the condenser is governed by Fick's diffusion law,[48,49]

$$\dot{m} = A_0 D \left[\frac{c_{sat}(T_e) - c_{sat}(T_c)}{t_a} \right], \qquad \text{(Equation 4)}$$

where D is the diffusivity of water vapor in air and c_{sat} is the saturation vapor mass concentration defined in Notes S2 and S3. Equations 2, 3, and 4 have three unknowns: T_e the evaporator membrane temperature, T_c the condenser membrane temperature, and $\dot{m}$ the mass flow rate, which is equal to the distillate production rate at steady state. The following section illustrates the numerical solutions of T_e, T_c, and $\dot{m}$, which will be validated using our experimental data. Subsequently, we conduct a detailed investigation into the impact of various design parameters on the solar-to-water efficiency.

Model validation

Since the actual geometry of the Ultem feature is complex (see Figure S12) and the heat conduction cannot be approximated using a 1D model, R_{side} is calculated in COMSOL (see Note S2 and Figure S13 for details) and we obtain R_{side} = 33.3 K/W. The rest of the thermal resistances can simply be calculated using Equations S5, S7, and S8. Using the thermophysical properties listed in Table S1, and an air convection heat transfer coefficient of $10\ \mathrm{W\,m^{-2}\,K^{-1}}$ on the bottom and top surfaces of the device, the numerical solution of Equations 2, 3, and 4 in MATLAB yields T_c = 51.65°C and T_e = 54.67°C, which are in a great agreement with the experimental results (Figures 3B and 3D). In addition, the solar-to-water efficiency calculated using Equation 1 is found to be 28.87%. These results are in excellent agreement with the experimentally observed values. Finally, a great agreement with only a 12% discrepancy has been observed between the theoretical mass rate (black dashed lines in Figures 3A and 3C) and the experimental data (pink data points). Note that the ambient temperature was set to 20°C and the mass diffusivity of water vapor in air was determined using Chapman-Enskog theory (see Note S3) as part of the analysis process.

To further validate the model for regimes with enhanced convective heat transfer coefficient on the condenser surface, we conducted an additional controlled experiment. The experiment involved a v1-condenser equipped with fins, referred to as v3-condenser, along with two side-by-side fans to increase the convective heat transfer coefficient. The experimental duration extended over 1 day to evaluate the desalination performance. Impressively, the results showcased outstanding consistency between the theoretical predictions and experimental findings, with a mere 5% error rate; please see the "Model validation via convective cooling experiment" section.

Parametric study

In this section, we utilized the model framework discussed in the previous section to investigate the influence of different parameters on the optimization of solar-to-water efficiency. The thermophysical properties are based on Table S1. It is worth noting that, for the purpose of our analysis, the calculation is for a scaled-up device such that $A_0 \gg A_{side}$. Therefore, Q_{side} is negligible and we did not include the $(T_e - T_{amb})/R_{side}$ term in Equation 2. By excluding Q_{side} from our calculations, we obtained the results and conclusions presented in Figures 4C–4E.

Figures 4C–4E illustrate the effects of various parameters on the solar-to-water efficiency, including the evaporator-condenser gap (t_a) and air convective heat transfer coefficients on the bottom surface of the condenser (h_{bottom}) and the top surface of the transparent film (h_{top}). As illustrated in Figure 4C, the system's efficiency decreases as the gap size between the evaporator and condenser increases. This phenomenon is primarily attributed to the elevated vapor transport resistance, which arises due to the expanded gap size between the two components. The impact of this decrease is more pronounced when there is a larger value (h_{bottom} = 50 W m^{-2} K^{-1}) of convective heat transfer coefficient at the bottom of the condenser.

We then examine the influence of the condenser total thermal resistance on the efficiency (Figure 4D) by varying h_{bottom}. For a natural air convective boundary condition on the top (h_{top} = 10 W m^{-2} K^{-1}), increasing h_{bottom} results in an increase in the efficiency. This is because when the total thermal resistance on the condenser side is decreased by increasing h_{bottom}, heat dissipation from the condenser to the environment is enhanced. Therefore, temperatures of the evaporator and the condenser are reduced, which decreases heat loss and enables better utilization of solar energy to evaporate water. As a result, the overall efficiency of the system improved, maximizing its ability to convert solar energy into usable heat for water heating purposes. These observations have been experimentally verified and validated through our modeling efforts (see the "Model validation via convective cooling experiment" section). Interestingly, as shown in Figure 4D, the efficiency reached a plateau at approximately $h_{\mathrm{bottom}} \approx$ 30 W m^{-2} K^{-1}. If we thermally insulate the top surface of the evaporator by setting h_{top} = 1 W m^{-2} K^{-1}, the solar-to-water efficiency of the system is much higher (>70%). This is because heat loss on the evaporator is suppressed. Interestingly, the efficiency for h_{top} = 1 W m^{-2} K^{-1} is relatively insensitive to h_{bottom}, and even decreases slightly, possibly due to minor uncertainty in the empirical vapor concentration equation. A maximum solar-to-water efficiency of 72.5% was achieved when h_{top} = 1 W m^{-2} K^{-1}. In an ideal scenario where the total solar energy is fully absorbed by the membrane and the transmittance of the top cover is 100% ($Q_{\mathrm{ab}} = q_{\mathrm{solar}}$), the efficiency could further increase to 90%. The importance of thermal insulation on the evaporator side is also shown in Figure 4E, where reducing h_{top} contributed to an increase of the efficiency. To enhance the system's overall performance and reduce energy losses during the conversion process, optimizing the top cover's transmittance, the evaporator membrane's absorptance, increasing the total thermal resistance on the top of the evaporator, and reducing the condenser's thermal resistance to the ambient air are crucial factors. These adjustments play a significant role in increasing the solar-to-water efficiency and maximizing the utilization of solar energy for water heating.

Model validation via convective cooling experiment

The provided modeling showcases how the thermal resistances affect the solar-to-water efficiency. Specifically, enhancing the convective heat transfer coefficient on the external surface of the condenser will increase the solar-to-water efficiency. To validate this, a comprehensive full-day passive test is conducted using the passive water-driven method (Figure 5), which involves positioning two identical 4 × 4 cm fans (Figure S8) that blow room temperature air to cool the bottom surface of the condenser. An air velocity of v_{air} = 2.5 m/s was measured (see experimental setup). It is experimentally observed that the increment in the convective heat transfer coefficient on the condenser surface has resulted in an increase in the solar-to-water efficiency to 39% (Figure 5A), and a decrease in the evaporator and condenser temperature (Figure 5B). The average condenser, evaporator, and ambient temperatures are ascertained to be $T_c \approx 29^{\circ}C$, $T_e \approx 40^{\circ}C$, and $T_{\mathrm{amb}} \approx 23\ ^{\circ}C$, respectively. To

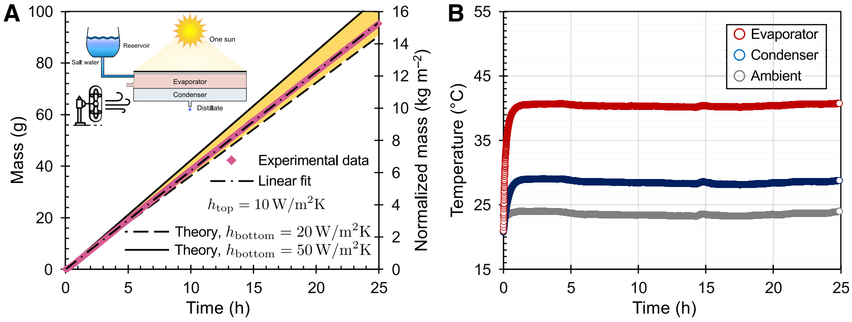

Figure 5. Comparative analysis between experimental and analytical predictions of the 1-day continuous experiment utilizing a gravity-driven water container and fans setup

Air velocity regulation beneath the condenser was achieved using two identical 4 × 4 cm fans (see Figures S8 and S9). The experiment was conducted in a controlled environment with an average temperature of $T_{\mathrm{amb}} \approx 23^{\circ}\mathrm{C}$ and a relative humidity of RH ≈ 60%. In (A) the continuous experimental distillate production over time is depicted by the pink data points, revealing a collection rate of 3.83 g h^{-1} (92 g day^{-1}). The orange region, bounded by two lines (dashed and solid), illustrates theoretical predictions for varying convective heat transfer coefficients from 20 (dashed line; $\eta = 37.5\%$) to 50 W m^{-2} K^{-1} (solid line; $\eta = 43.7\%$). Corresponding temperatures of the laboratory, condenser, and evaporator are recorded and plotted in (B).

validate the experimental result with the model, the thermophysical properties used are listed in Table S1. The convective heat transfer coefficient on the aluminum condenser can be roughly estimated as $h_{\mathrm{bottom}} = \frac{k_{\mathrm{air}}\,\overline{\mathrm{Nu}}}{\delta}$, where $\delta \sim \mathcal{O}(10\ \mathrm{cm})$ is the characteristic length, $k_{\mathrm{air}} \approx 0.03\ \mathrm{W\ m^{-1}\ K^{-1}}$ is thermal conductivity of air, and $\overline{\mathrm{Nu}}$ is the average Nusselt number and can be defined in terms of Prandtl (Pr = 0.71 for air) and Reynolds ($\mathrm{Re} = \frac{\rho_{\mathrm{air}} v_{\mathrm{air}} \delta}{\mu_{\mathrm{air}}}$) numbers as $\overline{\mathrm{Nu}} = 0.664 Re^{1/2}$. By utilizing the viscosity of air as $\mu_{\mathrm{air}} = 1.825 \times 10^{-5}$ Pa·s, we can calculate the convective heat transfer coefficient as $h_{\mathrm{bottom}} \approx 20\ \mathrm{W\ m^{-2}\ K^{-1}}$. Since the v3-condenser has fins that extend beyond the fans which promote convection, we used 50 and 20 W m^{-2} K^{-1} as the estimated upper and lower bounds of h_{bottom} and the results (dashed and solid lines) are shown in Figure 5A, which agrees reasonably well with the experimental results. In addition, the model predicts temperatures of the condenser and evaporator to be $T_c = 41.37^{\circ}\mathrm{C}$ and $T_e = 46.97^{\circ}\mathrm{C}$, which are in relative agreement with the experimental results. Although forced air convection was used here to illustrate the influence of h_{bottom}, other passive methods to increase h_{bottom} such as a device floating on the ocean and radiative cooling may be employed to reduce the thermal resistance R_{bottom}.

DISCUSSION

This 7-day desalination result is significant because it is the longest continuous solar desalination with passive salt rejection to date. Other works such as one by Wang et al. report continuous solar desalination with no salt accumulation for 12 h when using 7 wt % NaCl.[16] One work by Xu et al. reports salt accumulation and rejection over 18.5 h with illumination for 3 h using 3.5 wt % NaCl.[17] In addition, Ni et al. reports continuous solar vapor production from 3.5 wt % NaCl for 2000 s[18] (~0.55 h). These works reported these results under laboratory conditions and indicate that the result from our work is a contribution to the field.

As shown by the model, efficiency of our device can be improved by thermally insulating the top of the evaporator to reduce heat loss from the transparent cover to the ambient environment. This can be achieved using transparent and thermally insulating aerogels as the top cover, which has been implemented in several works.[17,50,51] In addition, the target flow rate of 5 mL h $^{-1}$ may be further reduced to reduce the convective heat loss in the water. At 5 mL h $^{-1}$, the equilibrium concentration of the salt water in the desalinator was 5.60 wt %, which is below saturation (26.889 wt %). At a reduced flow rate, a higher equilibrium evaporator temperature can potentially be established leading to higher vapor and distillate production. It is worth noting that salt water flows from a reservoir into the evaporator driven by gravity, not driven by the solar-flux-dependent evaporation rate. Therefore, implementing a passive mechanism to lower the flow rate during cloudy days or during the night for un-monitored operations may avoid consuming unnecessary salt water from the reservoir. The flow rate could potentially be regulated using a valve that responds to sunlight exposure. For example, we can add a pneumatically controlled valve that contains an amount of sealed air in contact with a black absorber surface. When the sun is out, the absorber absorbs sunlight and heats the air, which thermally expands. The expansion can cause the valve to open. When it is cloudy or at night, the absorber receives weaker or no light, and the air in the chamber contracts to close the valve.

On the condenser side, enhancing heat rejection from the aluminum surface to the ambient environment may also help to lower the condenser temperature and increase the efficiency. This can be achieved with increased aluminum surface area, or incorporating radiative cooling. Furthermore, efficiency can also be improved by a multi-stage design, where the condensation heat is re-used to evaporate water in the subsequent stage. The first stage will still be heated by sunlight; however, the remaining evaporation interfaces need to be thermally connected to the condenser. The backside of the condenser can be machined with grooves to allow the next-stage salt water to flow inside, and the hydrophobic evaporator membranes will be attached to the metal surface. The sensible heat of the discharged water can also be used to heat the next-stage salt water.

Furthermore, we introduce a novel thin-film condensation approach, which utilizes the highly effective three-phase contact region for phase change heat transfer, as well as a low vapor transport resistance by reducing the distance between the evaporation and the condensation surfaces. By demonstrating 7 days of continuous desalination we have achieved the longest continuous desalination among the reported solar thermal desalination full systems with salt rejection under one sun. This work presents a new architecture that addresses a long-standing problem of salt accumulation in current state-of-the-art solar thermal desalination devices, and highlights the importance of optimizing vapor transport and condensation in the overall efficiency of passive solar desalinators.

EXPERIMENTAL PROCEDURES

Resource availability

Lead contact

Further information and requests for resources and reagents should be directed to and will be fulfilled by the lead contact, Yangying Zhu (yangying@ucsb.edu).

Materials availability

This study did not generate new unique materials.

Data and code availability

- UV-Vis-NIR data, distillate production data, and temperature data have been deposited at Mendeley under https://doi.org/10.17632/hwxk9cxps9.1 and

are publicly available as of the date of publication. All other data reported in the supplemental information will be shared by the lead contact upon request.
- The MATLAB code generated for the model has been deposited at Mendeley under https://doi.org/10.17632/hwxk9cxps9.1 and is publicly available as of the date of publication.
- Any additional information required to reanalyze the data reported in this paper is available from the lead contact upon request.

Fabrication of the evaporator membrane

To enhance the optical absorptivity of the evaporator membrane, we followed a method reported by Liu et al.[52] The evaporator membrane fabrication is composed of two processes, membrane preparation and preparation of the coating solution. First the membrane is prepared. Carbon powder (0.8 g) (Sid Richardson Carbon & Energy) is dispensed into a 250 mL beaker containing 160 mL of water. Acetic acid (3 mL) is added to make the carbon powder easier to attach to fibers. The mixed solution is blended using an ultrasonic cleaner (Branson Ultrasonics Bransonic B200) for 5 min. The 110 mm diameter porous carbon paper (Toray Paper 060 TGP-H-060) is added to the mixed solution to vibrate for 3 min in order for the carbon powders to dye the paper uniformly. We dried the carbon immersed GDL at 80°C on a hotplate for 2 h. We repeated the membrane preparation process four times to realize the desired dark color.[52]

According to Liu et al., the coating solution is prepared by dispersing 1 g of PDMS containing 10% curing agent and 1 g of carbon black nanoparticles into 30 mL of hexane. The coating solution is mixed by a magnetic stir bar for 10 min. We immersed the membrane into the coating solution. Then, we cured the membrane on a hotplate at 80°C for 2 hours.[52]

Equipment setup and evaporator characterization

In all experiments, the grade AAA solar simulator by Newport ORIEL SOL3A illuminates the evaporator membrane with a solar flux of 1,000 W/m^2. For the desalination experiments (Figures 3 and 5), thermocouples (Omega J-Type, 5SRTC-TT-J-36-36) are used to measure the evaporator, condenser, and ambient air temperatures. The thermocouples are connected to a PC via an 8-Channel Benchtop Digital Thermometer Data Logger (Omega, DP9800-TC). The thermocouples are coated with a layer of thermally conductive epoxy (MG Chemicals 8349TFM Thermally Conductive 1 to 1 Epoxy Adhesive, Two Part 25 mL Dual Syringe). The cured epoxy is not water soluble, which allows for long duration temperature measurements at the condenser and evaporator.

To measure the vapor flux observed in Figure 2G, we supplied seawater with a salinity of 2.90 wt % to the desalinator device using a syringe pump (Cole Palmer, catalog no. 78-0100C) for 10 h. To estimate an upper limit of the solar-to-vapor efficiency corresponding to a minimal liquid flow rate, we used a syringe pump to supply salt water to the evaporator and gradually reduced the flow rate until the flow rate of the discharged water was negligibly low. At this condition, the inlet flow rate was 4.9 mL h^{-1} and the discharged flow rate was measured to be 0.18 mL h^{-1}. The mass of the evaporated liquid over time shown in Figure 2G was calculated by subtracting the mass of the discharged water measured using a mass balance from the mass of the supplied liquid. The salinity of the seawater on the evaporator membrane was 3.32 wt % after 10 h and no salt crystals formed on the evaporator membrane during this duration. We used a Shimadzu UV3600 UV-Vis-NIR Spectrometer to measure the transmittance of the PETG and ETFE films and the reflectance of the evaporator membrane. To calculate the absorptance of the dark evaporator membrane we approximated transmittance to be zero and subtracted the reflectance from one.

Fully passive gravity-driven solar desalinator setup

In the passive desalination test (Figure 3A), we use a passive flow source. Salt water from Goleta Beach is supplied using a 2-gallon water bottle (New Wave Enviro Polycarbonate Water Bottle, 2-Gallon, Screw Top Cap with Integrated Handle for Easy Carrying, Built for Durability, Blue [B09VTL5Q65]) which provides gravity driven flow with no energy consumption. The flow rate is measured by massing the distillate and outlet discharge over time. For the first passive desalination test, the water bottle flow rate varies from 10.82 to 4.5 mL h^{-1} over the duration of the 7-day experiment and was refilled once during day 3 (see Figure S4). To achieve these low flow rates and allow any sediment present in the salt water to pass through the device, 10 m of 1/16 inch (ID) tubing is connected between the water bottle and the inlet of the desalinator to provide hydraulic resistance. At the maximum flow rate, the height difference between the outlet of the desalinator and the water level in the water bottle is 2.7 cm. The detailed experimental setup is shown in Figure S3.

Syringe pump-driven solar desalinator setup

In Figure 3C, saltwater is supplied to the desalinator device using a syringe pump (Harvard Apparatus Pump 33DDS, 70-3333) with a controlled flow rate of 5 mL h^{-1}. The syringe pump drives flow actively into the desalinator inlet. To dispel salt water from the device, the inlet flow rate is greater than the distillate rate. The salt concentration within the desalinator does not exceed 26.889 wt %, the saturation concentration for salt in water. The detailed experimental setup is shown in Figure S7. Two mass balances (OHAUS Scout STX2202 and STX123) are used in conjunction with OHAUS serial port data collection to measure the distillate mass and outlet discharge mass at a 10 s sample frequency.

Fully passive gravity-driven solar desalinator model validation setup

For the model validation passive desalination test setup (Figure S9), we use the identical passive source setup as illustrated in Figure S9A. The flow rate varied from 6.04 to 4.12 mL h^{-1} over the duration of the 25 h test as shown in Figure S10. Two fans (ebmpapst, 412 FM) are added to cool the condenser and a wind speed meter (PCE Instruments, PCE-HWA 20BT) is used to measure the wind velocity. An air shield is constructed above the condenser to prevent air from the fan from reaching the evaporator.

SUPPLEMENTAL INFORMATION

Supplemental information can be found online at https://doi.org/10.1016/j.xcrp.2023.101682.

ACKNOWLEDGMENTS

This work was supported by the National Science Foundation under grant no. 2047727 and a seed fund from the Institute for Energy Efficiency at University of California, Santa Barbara. Patrick Babb acknowledges the National Science Foundation Graduate Research Fellowship Program (GRFP), grant no. 2139319. The authors thank Marty Ramirez for supervising the manufacturing of the desalinator device, and Aleks Labuda who machined a preliminary desalinator. The authors acknowledge the Materials Department at UCSB for providing the SEM equipment. The authors acknowledge the Materials Research Laboratory for providing the UV-Vis-NIR equipment. The MRL Shared Experimental Facilities are supported by the MRSEC Program of the NSF under award no. DMR 2308708; a member of the NSF-funded Materials Research Facilities Network (http://www.mrfn.org). The authors acknowledge the use of the Innovation Workshop within the California NanoSystems Institute, supported by the University of California, Santa Barbara and the University of California, Office of the President.

AUTHOR CONTRIBUTIONS

P.I.B. and S.F.A. contributed equally to this work. S.F.A. and Y.Z. ideated and developed the initial prototype. P.I.B. performed the experiments. S.F.A. and P.I.B. analyzed the data. S.F.A. and Y.Z. developed the theoretical modeling. F.B., R.G., M.A.L., J.S., Q.W., and B.Z. designed and fabricated a scaled-up desalinator under the supervision of K.F. and T.S. F.B. developed a prototype model, sourced materials, and led manufacturing with contributions from B.Z. and R.G. J.S. and Q.W. manufactured a test stand. X.Z. contributed to fabrication and collection of salt water. A.S., J.N., and P.I.B. conducted the absorptivity measurement. P.I.B. conducted the transmissivity measurements and took the SEM images. All authors discussed and contributed to the writing and revision of this paper.

DECLARATION OF INTERESTS

Y.Z. and P.I.B. have an interest in a US provisional patent application related to this publication.

INCLUSION AND DIVERSITY

We support inclusive, diverse, and equitable conduct of research. One or more of the authors of this paper self-identifies as an underrepresented ethnic minority in their field of research or within their geographical location. One or more of the authors of this paper self-identifies as a gender minority in their field of research. One or more of the authors of this paper received support from a program designed to increase minority representation in their field of research.

Received: April 14, 2023
Revised: October 11, 2023
Accepted: October 23, 2023
Published: November 15, 2023

REFERENCES

1. Van der Bruggen, B. (2003). Desalination by distillation and by reverse osmosis — trends towards the future. Membr. Technol. *2003*, 6–9. https://doi.org/10.1016/S0958-2118(03)02018-4.
2. Ghalavand, Y., Hatamipour, M.S., and Rahimi, A. (2014). A review on energy consumption of desalination processes. Desalination Water Treat. 1–16. https://doi.org/10.1080/19443994.2014.892837.
3. Neumann, O., Urban, A.S., Day, J., Lal, S., Nordlander, P., and Halas, N.J. (2013). Solar vapor generation enabled by nanoparticles. ACS Nano *7*, 42–49. https://doi.org/10.1021/nn304948h.
4. Seckler, D., Barker, R., and Amarasinghe, U. (1999). Water Scarcity in the Twenty-first Century. Int. J. Water Resour. Dev. *15*, 29–42. https://doi.org/10.1080/07900629948916.
5. Ghasemi, H., Ni, G., Marconnet, A.M., Loomis, J., Yerci, S., Miljkovic, N., and Chen, G. (2014). Solar steam generation by heat localization. Nat. Commun. *5*, 4449. https://doi.org/10.1038/ncomms5449.
6. Zhou, L., Tan, Y., Wang, J., Xu, W., Yuan, Y., Cai, W., Zhu, S., and Zhu, J. (2016). 3D self-assembly of aluminium nanoparticles for plasmon-enhanced solar desalination. Nat. Photonics *10*, 393–398. https://doi.org/10.1038/nphoton.2016.75.
7. Tao, P., Ni, G., Song, C., Shang, W., Wu, J., Zhu, J., Chen, G., and Deng, T. (2018). Solar-driven interfacial evaporation. Nat. Energy *3*, 1031–1041. https://doi.org/10.1038/s41560-018-0260-7.
8. Ni, G., Li, G., Boriskina, S., Li, H., Yang, W., Zhang, T., and Chen, G. (2016). Steam generation under one sun enabled by a floating structure with thermal concentration. Nat. Energy *1*, 16126. https://doi.org/10.1038/nenergy.2016.126.
9. Dong, X., Si, Y., Chen, C., Ding, B., and Deng, H. (2021). Reed Leaves Inspired Silica Nanofibrous Aerogels with Parallel-Arranged Vessels for Salt-Resistant Solar Desalination. ACS Nano *15*, 12256–12266. https://doi.org/10.1021/acsnano.1c04035.
10. Zhou, X., Zhao, F., Guo, Y., Zhang, Y., and Yu, G. (2018). A hydrogel-based antifouling solar evaporator for highly efficient water desalination. Energy Environ. Sci. *11*, 1985–1992. https://doi.org/10.1039/C8EE00567B.
11. Zhao, F., Zhou, X., Shi, Y., Qian, X., Alexander, M., Zhao, X., Mendez, S., Yang, R., Qu, L., and Yu, G. (2018). Highly efficient solar vapour generation via hierarchically nanostructured

gels. Nat. Nanotechnol. *13*, 489–495. https://doi.org/10.1038/s41565-018-0097-z.

12. Menon, A.K., Haechler, I., Kaur, S., Lubner, S., and Prasher, R.S. (2020). Enhanced solar evaporation using a photo-thermal umbrella for wastewater management. Nat. Sustain. *3*, 144–151. https://doi.org/10.1038/s41893-019-0445-5.
13. Xu, N., Li, J., Wang, Y., Fang, C., Li, X., Wang, Y., Zhou, L., Zhu, B., Wu, Z., Zhu, S., and Zhu, J. (2019). A water lily-inspired hierarchical design for stable and efficient solar evaporation of high-salinity brine. Sci. Adv. *5*, eaaw7013.
14. Xu, N., Zhang, H., Lin, Z., Li, J., Liu, G., Li, X., Zhao, W., Min, X., Yao, P., Zhou, L., et al. (2021). A scalable fish-school inspired self-assembled particle system for solar-powered water-solute separation. Natl. Sci. Rev. *8*, nwab065. https://doi.org/10.1093/nsr/nwab065.
15. Li, X., Ni, G., Cooper, T., Xu, N., Li, J., Zhou, L., Hu, X., Zhu, B., Yao, P., and Zhu, J. (2019). Measuring Conversion Efficiency of Solar Vapor Generation. Joule *3*, 1798–1803. https://doi.org/10.1016/j.joule.2019.06.009.
16. Wang, F., Xu, N., Zhao, W., Zhou, L., Zhu, P., Wang, X., Zhu, B., and Zhu, J. (2021). A high-performing single-stage invert-structured solar water purifier through enhanced absorption and condensation. Joule *5*, 1602–1612. https://doi.org/10.1016/j.joule.2021.04.009.
17. Xu, Z., Zhang, L., Zhao, L., Li, B., Bhatia, B., Wang, C., Wilke, K.L., Song, Y., Labban, O., Lienhard, J.H., et al. (2020). Ultrahigh-efficiency desalination: Via a thermally-localized multistage solar still. Energy Environ. Sci. *13*, 830–839. https://doi.org/10.1039/c9ee04122b.
18. Ni, G., Zandavi, S.H., Javid, S.M., Boriskina, S.V., Cooper, T.A., and Chen, G. (2018). A salt-rejecting floating solar still for low-cost desalination. Energy Environ. Sci. *11*, 1510–1519. https://doi.org/10.1039/C8EE00220G.
19. Dongare, P.D., Alabastri, A., Pedersen, S., Zodrow, K.R., Hogan, N.J., Neumann, O., Wu, J., Wang, T., Deshmukh, A., Elimelech, M., et al. (2017). Nanophotonics-enabled solar membrane distillation for off-grid water purification. Proc. Natl. Acad. Sci. USA *114*, 6936–6941. https://doi.org/10.1073/pnas.1701835114.
20. Xue, G., Chen, Q., Lin, S., Duan, J., Yang, P., Liu, K., Li, J., and Zhou, J. (2018). Highly Efficient Water Harvesting with Optimized Solar Thermal Membrane Distillation Device. Glob. Chall. *2*, 1800001. https://doi.org/10.1002/gch2.201800001.
21. Chiavazzo, E., Morciano, M., Viglino, F., Fasano, M., and Asinari, P. (2018). Passive solar high-yield seawater desalination by modular and low-cost distillation. Nat. Sustain. *1*, 763–772. https://doi.org/10.1038/s41893-018-0186-x.
22. Xu, N., Li, J., Finnerty, C., Song, Y., Zhou, L., Zhu, B., Wang, P., Mi, B., and Zhu, J. (2023). Going beyond efficiency for solar evaporation. Nat. Water *1*, 494–501. https://doi.org/10.1038/s44221-023-00086-5.
23. Wang, W., Shi, Y., Zhang, C., Li, R., Wu, M., Zhuo, S., Aleid, S., and Wang, P. (2021). Solar Seawater Distillation by Flexible and Fully Passive Multistage Membrane Distillation. Nano Lett. *21*, 5068–5074. https://doi.org/10.1021/acs.nanolett.1c00910.
24. Huang, L., Jiang, H., Wang, Y., Ouyang, Z., Wang, W., Yang, B., Liu, H., and Hu, X. (2020). Enhanced water yield of solar desalination by thermal concentrated multistage distiller. Desalination *477*, 114260. https://doi.org/10.1016/j.desal.2019.114260.
25. Zhang, L., Li, X., Zhong, Y., Leroy, A., Xu, Z., Zhao, L., and Wang, E.N. (2022). Highly efficient and salt rejecting solar evaporation via a wick-free confined water layer. Nat. Commun. *13*, 849. https://doi.org/10.1038/s41467-022-28457-8.
26. Morciano, M., Fasano, M., Boriskina, S.V., Chiavazzo, E., and Asinari, P. (2020). Solar passive distiller with high productivity and Marangoni effect-driven salt rejection. Energy Environ. Sci. *13*, 3646–3655. https://doi.org/10.1039/D0EE01440K.
27. Ma, J., Cha, H., Kim, M.K., Cahill, D.G., and Miljkovic, N. (2019). Condensation Induced Delamination of Nanoscale Hydrophobic Films. Adv. Funct. Mater. *29*. https://doi.org/10.1002/adfm.201905222.
28. Cohen, N., Dotan, A., Dodiuk, H., and Kenig, S. (2016). Superhydrophobic Coatings and Their Durability. Mater. Manuf. Process. *31*, 1143–1155. https://doi.org/10.1080/10426914.2015.1090600.
29. Said, I.A., Fuentes, N., He, Z., Xin, R., Zuo, K., and Li, Q. (2020). Low-cost desalination of seawater and hypersaline brine using nanophotonics enhanced solar energy membrane distillation. Environ. Sci. *6*, 2180–2196. https://doi.org/10.1039/d0ew00254b.
30. Rice, D., Ghadimi, S.J., Barrios, A.C., Henry, S., Walker, W.S., Li, Q., and Perreault, F. (2020). Scaling Resistance in Nanophotonics-Enabled Solar Membrane Distillation. Environ. Sci. Technol. *54*, 2548–2555. https://doi.org/10.1021/acs.est.9b07622.
31. Said, I.A., Fuentes, N., He, Z., Xin, R., Zuo, K., Walker, W.S., and Li, Q. (2021). Treatment of brackish water reverse osmosis brine using only solar energy. Environ. Sci. *7*, 1840–1851. https://doi.org/10.1039/d1ew00291k.
32. Oh, J., Zhang, R., Shetty, P.P., Krogstad, J.A., Braun, P.V., and Miljkovic, N. (2018). Thin Film Condensation on Nanostructured Surfaces. Adv. Funct. Mater. *28*. https://doi.org/10.1002/adfm.201707000.
33. Shan, L., Guo, Z., Monga, D., Boylan, D., and Dai, X. (2023). Microchannel-elevated micromembrane for sustainable phase-separation condensation. Joule *7*, 168–182. https://doi.org/10.1016/j.joule.2022.11.010.
34. Preston, D.J., Wilke, K.L., Lu, Z., Cruz, S.S., Zhao, Y., Becerra, L.L., and Wang, E.N. (2018). Gravitationally Driven Wicking for Enhanced Condensation Heat Transfer. Langmuir *34*, 4658–4664. https://doi.org/10.1021/acs.langmuir.7b04203.
35. (2023). Toray Carbon Paper 060. Wet Proofed. https://www.fuelcellstore.com/fuel-cell-components/gas-diffusion-layers/carbon-paper/toray-carbon-paper/toray-carbon-paper-060
36. (2023). TechniCloth® TX609 Nonwoven Dry Cleanroom Wipers. Non-Sterile. https://www.texwipe.com/technicloth-tx609
37. Rachid, A., Goren, A., Becerra, V., Radulovic, J., and Khanna, S. (2023). Fundamentals of Solar Energy, pp. 1–15. https://doi.org/10.1007/978-3-031-20830-0_1.
38. Pinho, S.P., and Macedo, E.A. (2005). Solubility of NaCl, NaBr, and KCl in Water, Methanol, Ethanol, and Their Mixed Solvents. J. Chem. Eng. Data *50*, 29–32. https://doi.org/10.1021/je049922y.
39. Zhu, L., Gao, M., Peh, C.K.N., and Ho, G.W. (2019). Recent progress in solar-driven interfacial water evaporation: Advanced designs and applications. Nano Energy *57*, 507–518. https://doi.org/10.1016/j.nanoen.2018.12.046.
40. Zhang, P., Li, J., Lv, L., Zhao, Y., and Qu, L. (2017). Vertically Aligned Graphene Sheets Membrane for Highly Efficient Solar Thermal Generation of Clean Water. ACS Nano *11*, 5087–5093. https://doi.org/10.1021/acsnano.7b01965.
41. Liu, Z., Song, H., Ji, D., Li, C., Cheney, A., Liu, Y., Zhang, N., Zeng, X., Chen, B., Gao, J., et al. (2017). Extremely Cost-Effective and Efficient Solar Vapor Generation under Nonconcentrated Illumination Using Thermally Isolated Black Paper. Glob. Chall. *1*, 1600003. https://doi.org/10.1002/gch2.201600003.
42. Li, X., Xie, W., and Zhu, J. (2022). Interfacial Solar Steam/Vapor Generation for Heating and Cooling. Adv. Sci. *9*, 2104181. https://doi.org/10.1002/advs.202104181.
43. Zhou, P., Zhu, Q., Sun, X., Liu, L., Cai, Z., and Xu, J. (2023). Recent advances in MXene-based membrane for solar-driven interfacial evaporation desalination. Chem. Eng. J. *464*, 142508. https://doi.org/10.1016/j.cej.2023.142508.
44. Sinhamahapatra, A., and Kumar, A. (2023). Review of the progress of solar-driven interfacial water evaporation (SIWE) toward a practical approach. Energy Adv. *2*, 574–605. https://doi.org/10.1039/D3YA00028A.
45. Wang, J., Wang, R., Geng, Y., Li, Y., Li, J., Qiu, J., and Li, M. (2023). Activated pulverized coal membrane for effective solar-driven interfacial evaporation and desalination. Chem. Eng. Sci. *265*, 118248. https://doi.org/10.1016/j.ces.2022.118248.
46. Wang, Y., Li, W., Wei, Y., and Chen, Q. (2023). Recyclable Monolithic Vitrimer Foam for High-Efficiency Solar-Driven Interfacial Evaporation. ACS Appl. Mater. Interfaces *15*, 14379–14387. https://doi.org/10.1021/acsami.2c23197.
47. Li, S., Qiu, F., Xia, Y., Chen, D., and Jiao, X. (2022). Integrating a Self-Floating Janus TPC@CB Sponge for Efficient Solar-Driven Interfacial Water Evaporation. ACS Appl. Mater. Interfaces *14*, 19409–19418. https://doi.org/10.1021/acsami.2c01359.
48. Fick, A. (1855). On liquid diffusion. London, Edinburgh Dublin Phil. Mag. J. Sci. *10*, 30–39. https://doi.org/10.1080/14786445508641925.

49. Bird, R.B., Stewart, W.E., and Lightfoot, E.N. (2006). Transport Phenomena, 2nd ed. (John Wiley & Sons).

50. Yu, X., Huang, M., Wang, X., Tang, G.H., and Du, M. (2023). Plasmon silica aerogel for improving high-temperature solar thermal conversion. Appl. Therm. Eng. *219*, 119419. https://doi.org/10.1016/j.applthermaleng.2022.119419.

51. Rastgar, M., Jiang, L., Wang, C., and Sadrzadeh, M. (2022). Aerogels in passive solar thermal desalination: a review. J. Mater. Chem. A Mater. *10*, 17857–17877. https://doi.org/10.1039/D2TA05216D.

52. Liu, Y., Chen, J., Guo, D., Cao, M., and Jiang, L. (2015). Floatable, Self-Cleaning, and Carbon-Black-Based Superhydrophobic Gauze for the Solar Evaporation Enhancement at the Air-Water Interface. ACS Appl. Mater. Interfaces *7*, 13645–13652. https://doi.org/10.1021/acsami.5b03435.

Cell Reports Physical Science, Volume *4*

Supplemental information

Salt-rejecting continuous passive solar thermal desalination via convective flow and thin-film condensation

Patrick I. Babb, S. Farzad Ahmadi, Forrest Brent, Ruby Gans, Mabel Aceves Lopez, Jiuxu Song, Qixian Wang, Brandon Zou, Xiangying Zuo, Amanda Strom, Jaya Nolt, Tyler Susko, Kirk Fields, and Yangying Zhu

Supplemental Note S.1: Device images and experimental setup

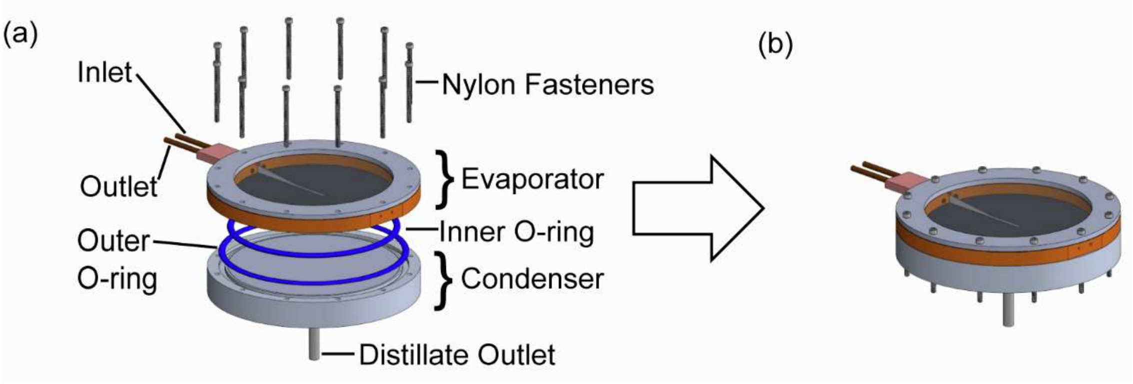

Figure S1. Isometric views of the desalinator. (a) Expanded view illustrating components used to assemble the desalinator. (b) Assembled desalinator used in tests.

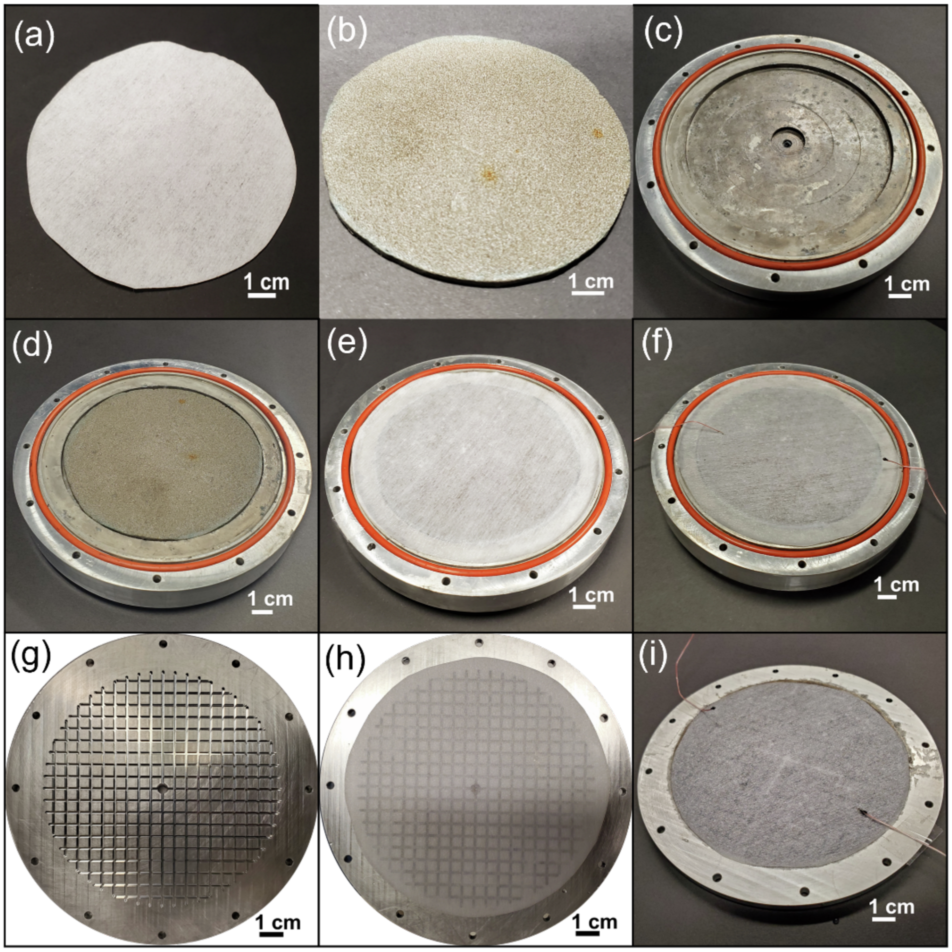

Figure S2. Condensers and condenser membranes. (a) microporous paper. (b) nickel foam. (c) aluminum v2-condenser (d) nickel foam in aluminum v2-condenser. (e) microporous paper on nickel foam on aluminum v2-condenser. (f) thermocouples on v2-condenser. (g) aluminum v1-condenser with channels. (h) microporous paper on aluminum v1-condenser with channels. (i) thermocouples on v1-condenser.

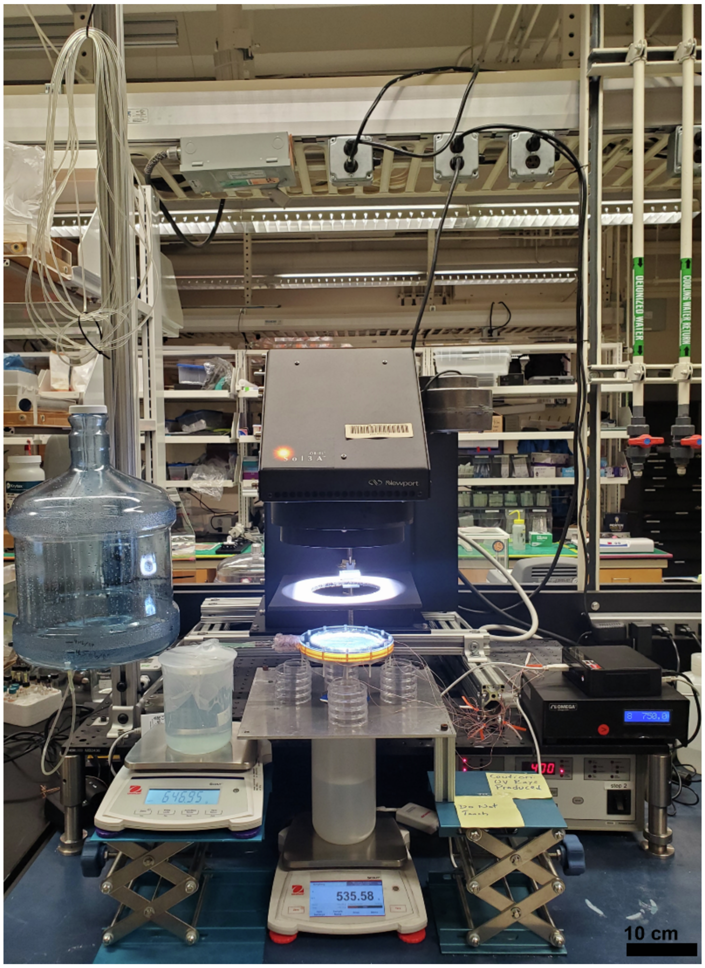

Figure S3. Image of the 7-day fully-passive gravity-driven solar desalinator using v1-condenser.

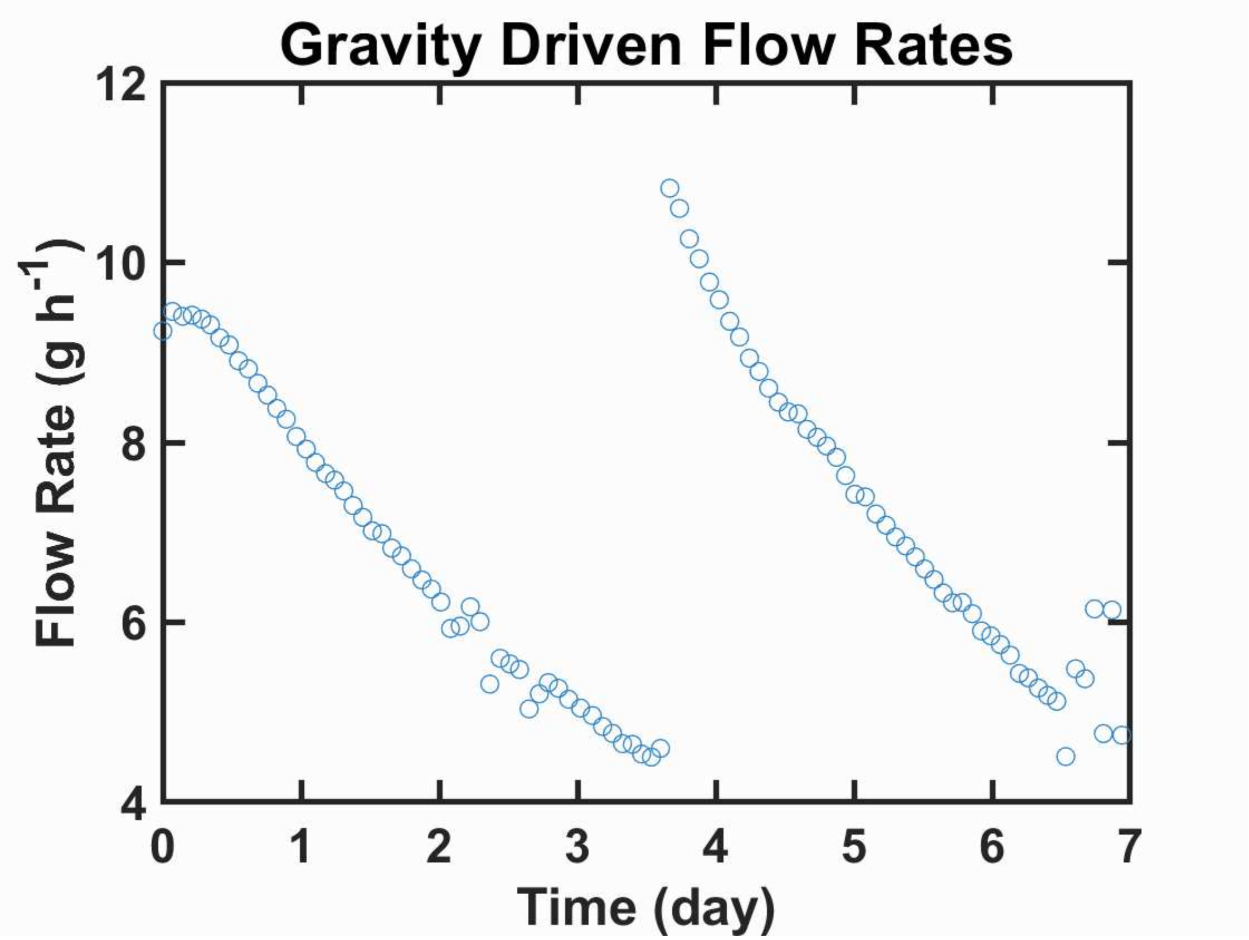

Figure S4. Flow rates from water bottle during the first 7-day fully-passive gravity-driven solar desalinator using v1-condenser. The gravity driven water bottle flow decreased in 2 cycles during the course of 7 days due to a decrease in the available hydrostatic pressure as salt water flows from the water bottle to the desalinator. The average flow rate over the duration of the test was 7 g h^{-1}. The flow rate from the water bottle was increased by adding the same mass of dispelled water back to the water bottle during day 3 of the experiment.

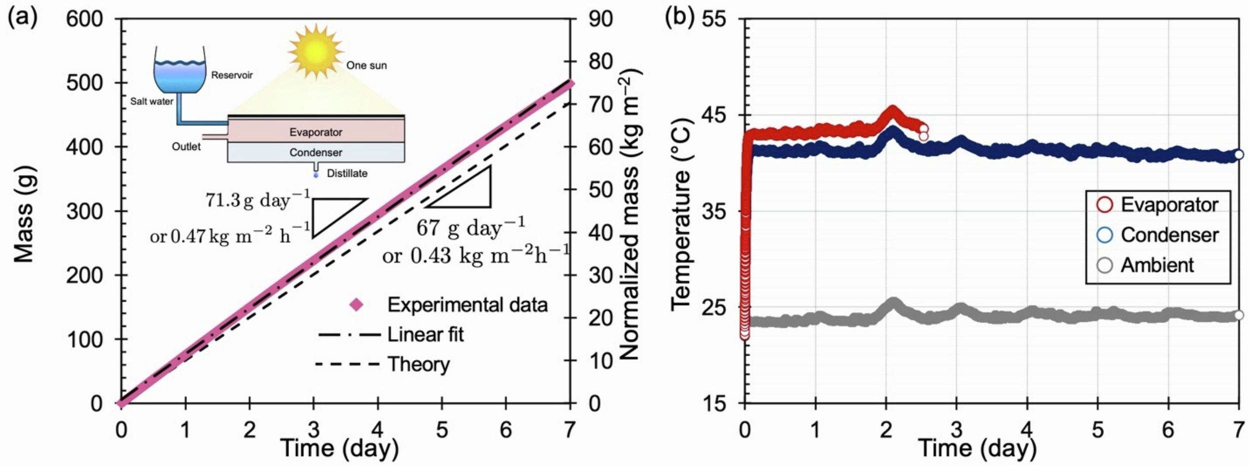

Figure S5. Second 7-day performance analysis of the device utilizing saline seawater and solar flux of 1000 W m^{-2}. This approach used fully passive gravity-driven water container testing (a) Inlet seawater salinity recorded at 3.15 wt%. The average inlet flow rate over the duration of the test was 7.2 g h^{-1}. During the full passive gravity-driven water container testing, the experiment entailed continuous monitoring of the mass rate (pink data points in a) and corresponding temperatures of the ambient, condenser, and evaporator (b). The fully passive experiment was conducted in a laboratory setting with an average temperature of $T_{\mathrm{amb}} \approx 24$ ºC and a relative humidity of $RH \approx 56\%$.

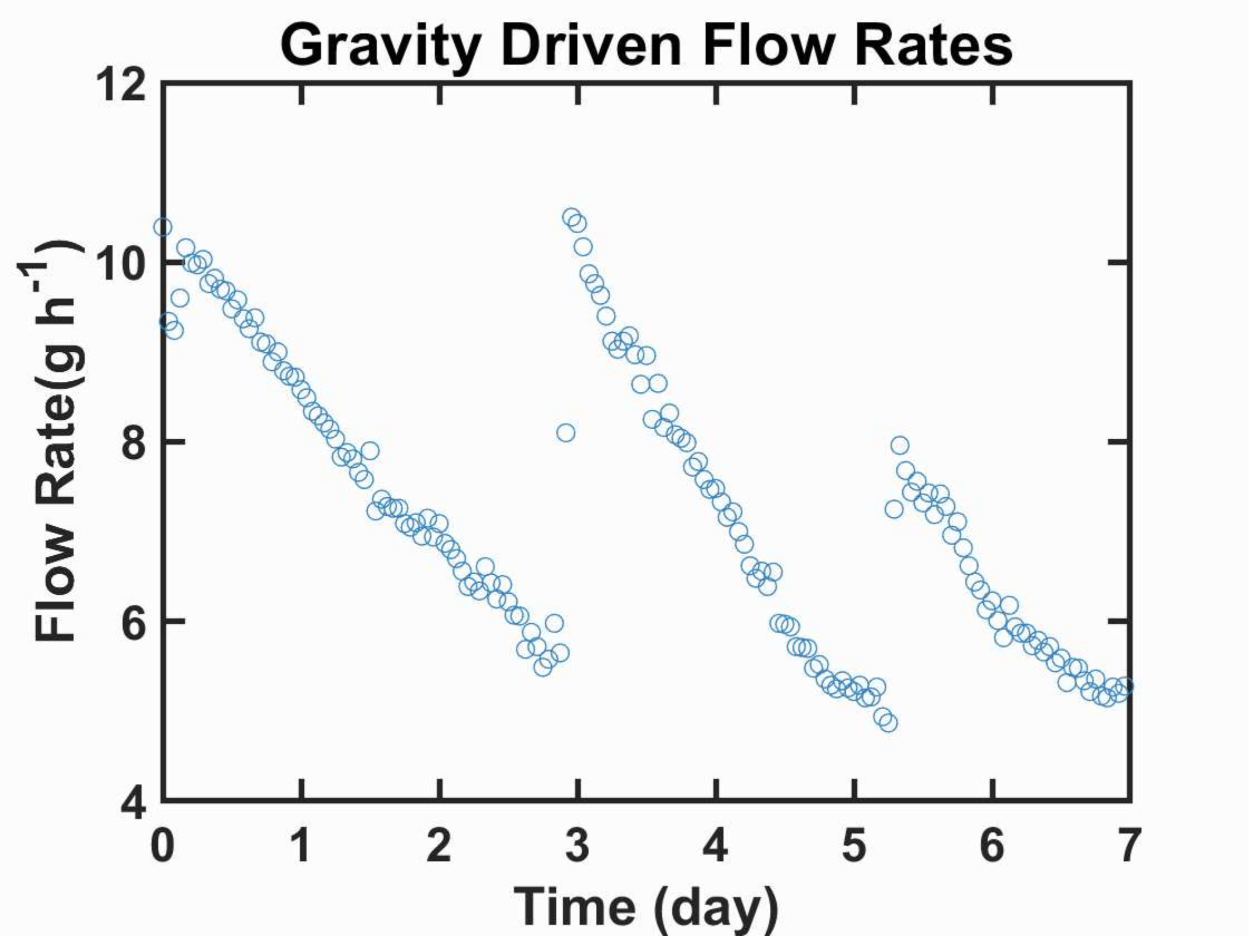

Figure S6. Flow rates from water bottle during the second 7-day fully-passive gravity-driven solar desalinator using v1-condenser. The gravity driven water bottle flow decreased in 3 cycles during the course of 7 days due to a decrease in the available hydrostatic pressure as salt water flows from the water bottle to the desalinator. The average flow rate over the duration of the test was 7.2 g h^{-1}. The flow rate from the water bottle was increased by adding sea water back to the water bottle during day 3 and day 5 of the experiment.

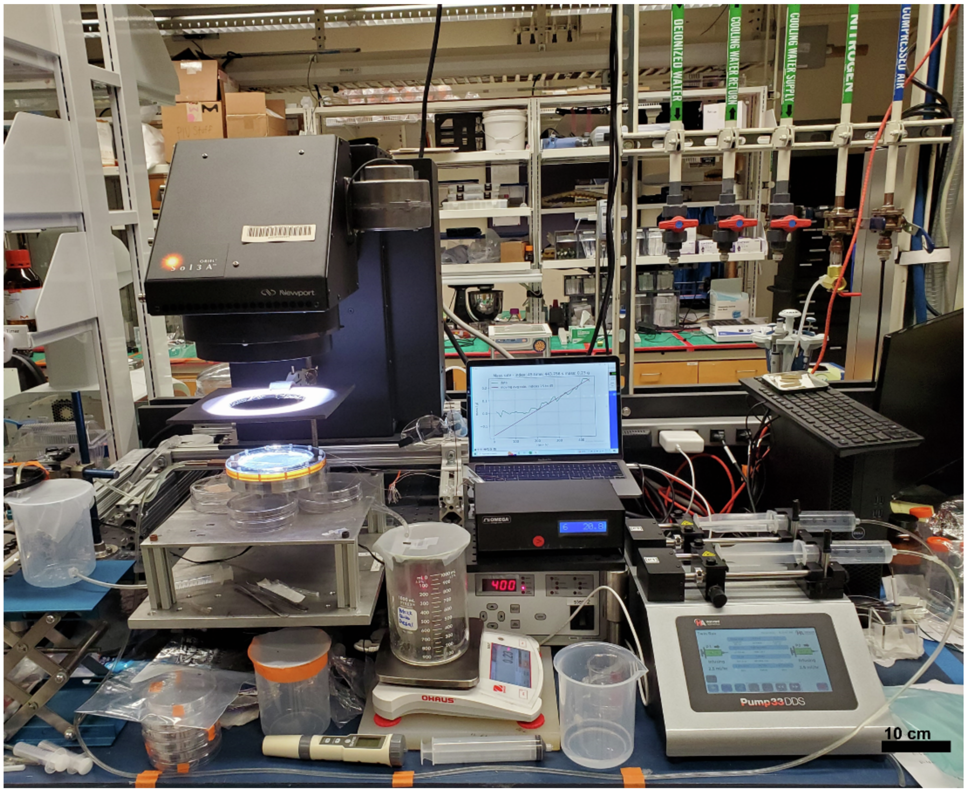

Figure S7. Image of 7-day solar desalinator experiment with syringe pump flow control under solar simulator in the lab. The syringe pump provided a controlled inlet flow rate of 5 ml h^{-1}.

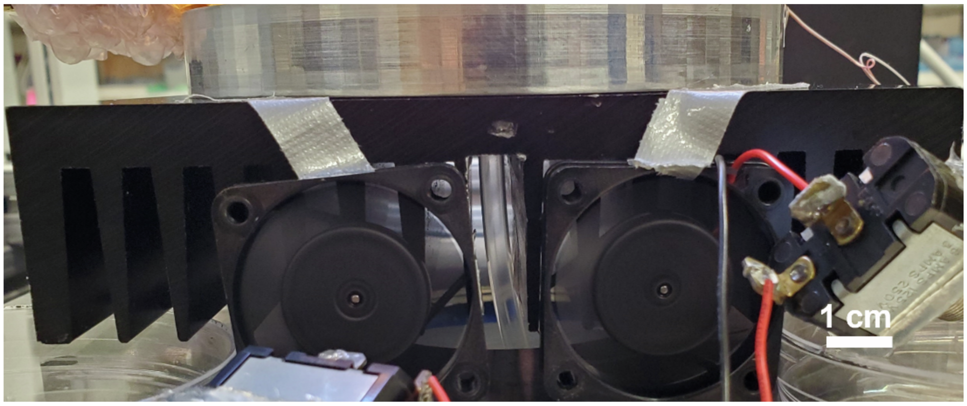

Figure S8. Image of the gravity-driven solar desalinator experiment with two 4 cm × 4 cm fans blowing air to the v3-condenser.

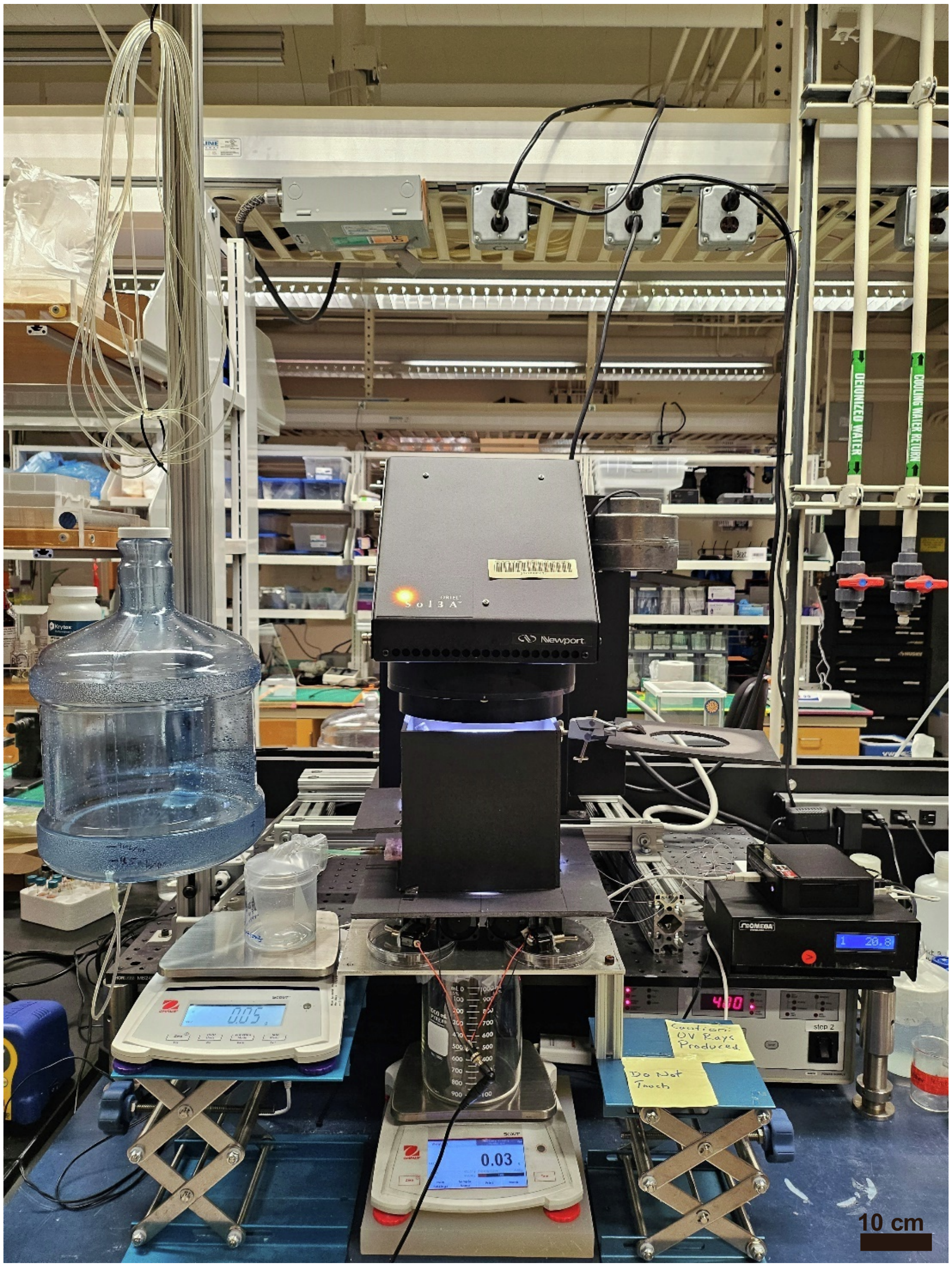

Figure S9. Image of the 1-day gravity-driven solar desalinator with convective cooling using v3-condenser. An air shield is constructed around the desalinator to prevent air flow from the fan reaching the evaporator.

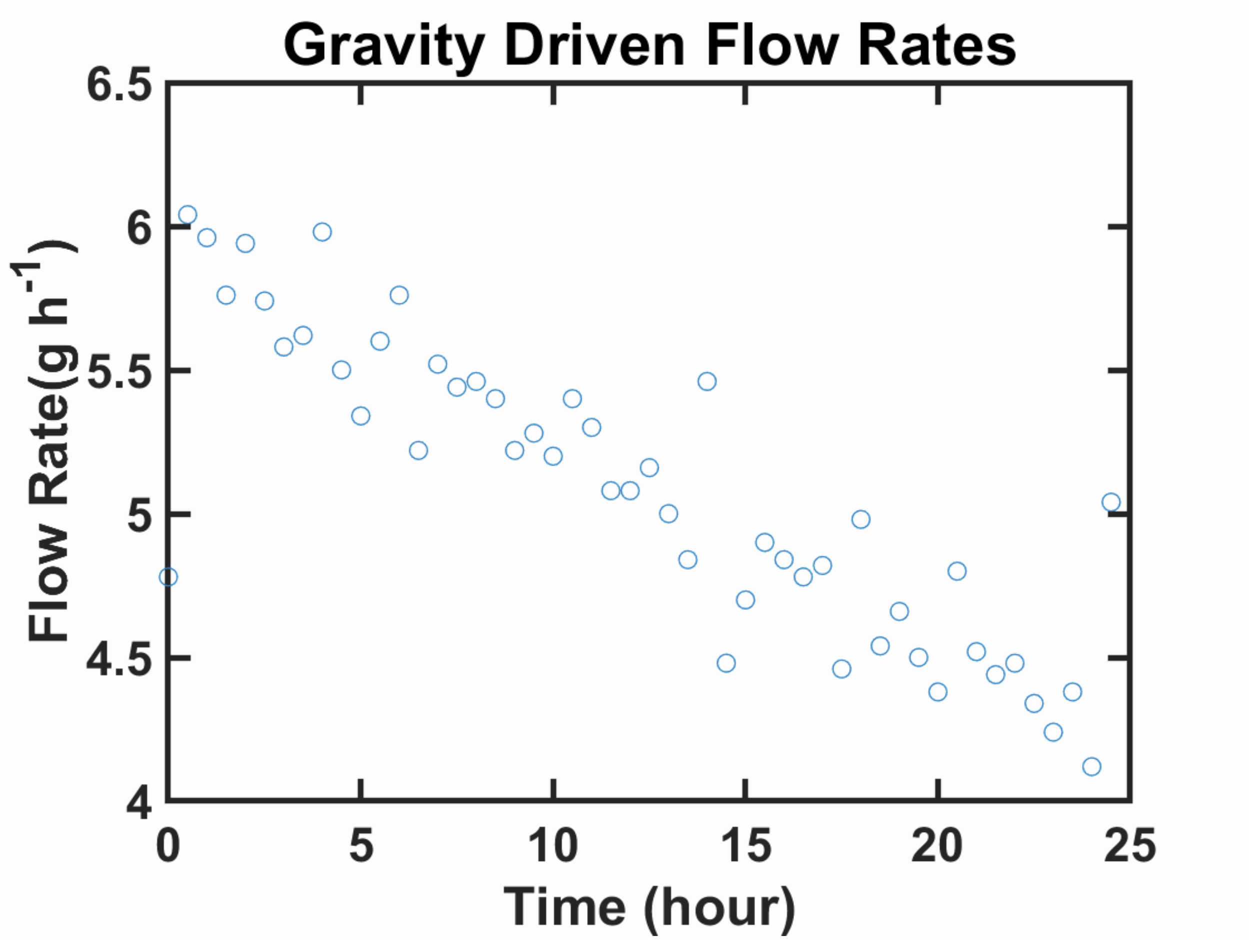

Figure S10. Flow rates from water bottle during the 1-day gravity-driven solar desalinator with convective cooling using v3-condenser. The average flow rate over the duration of the test was 4.9 g h^{-1}.

Supplemental Note S.2: Heat and mass transfer model and validation

In this section we aim to develop a heat and mass transport model to understand the energy (heat) loss observed in our system. The model will be validated using our experimental result, and we will then vary design parameters to investigate their effects on the solar-to-water efficiency.

A. Model framework

Figure S11 illustrates the cross-sectional view of the device. In the evaporator, there is a thin water layer with a thickness of h and a diameter of d. The top of the water layer contacts an ETFE film (0.127 mm in thickness), and the bottom of the water layer contacts the evaporator membrane, (i.e., the solar absorber). A plastic fixture made of Ultem material is positioned to come into contact with the side of the water film. This fixture serves as a boundary element within the system. Not depicted in Figure S11, there exists a Buna-N rubber O-ring that separates the evaporator membrane from the condenser membrane. The O-ring has a compressed thickness of approximately 3 mm and an uncompressed thickness of 3.5 mm. Moving to the condenser side, the condenser membrane directly interfaces with a porous metal structure, which can be either nickel foam or aluminum with open channels, and has a depth of 3 mm. The remaining portion of the condenser consists of an aluminum block, which maintains contact with the surrounding ambient air. For a comprehensive understanding of the device's dimensions, please refer to Figure S12, where a detailed drawing of the apparatus is provided, featuring all dimensions appropriately labeled.

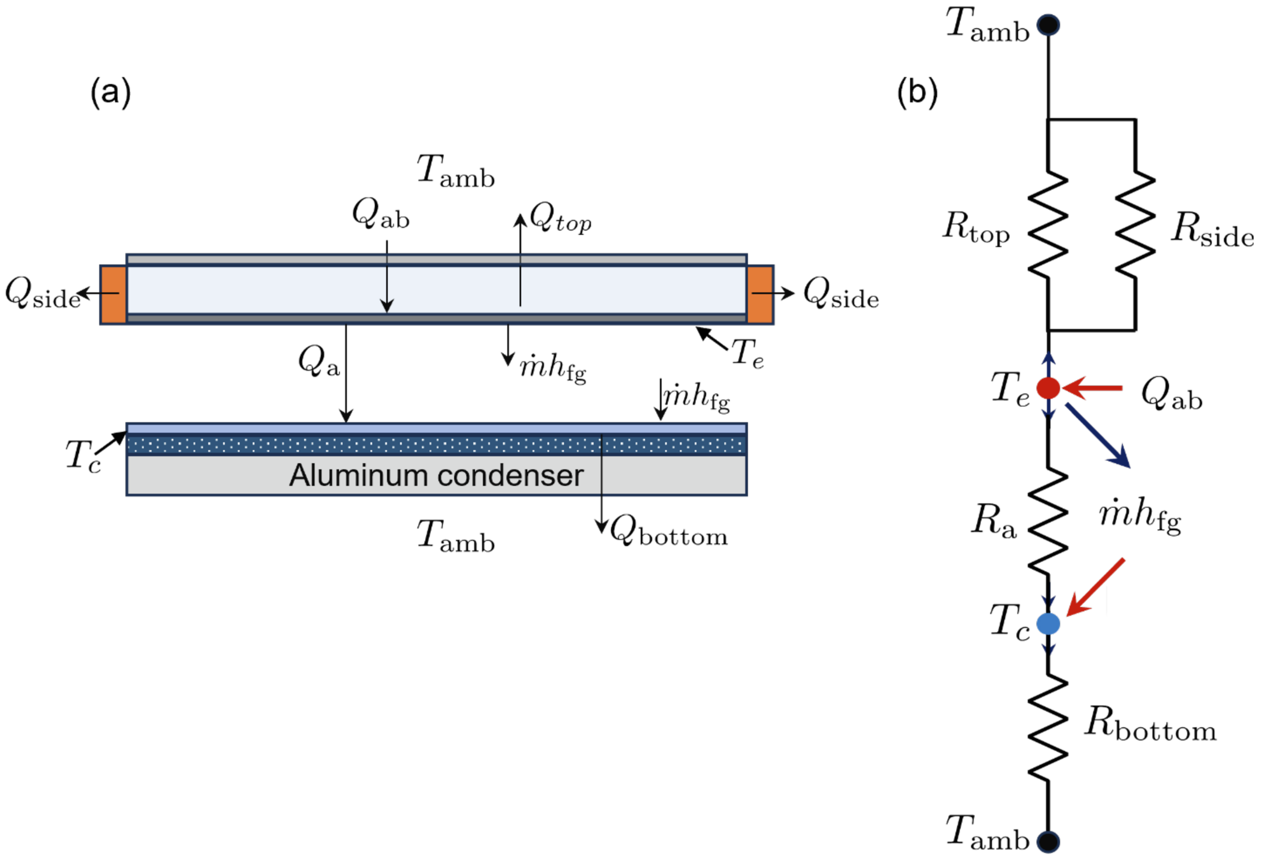

Figure S11. An overview of the heat transfer through the device. (a) Schematic of the cross section of the device and energy flow. (b) The equivalent thermal resistance network.

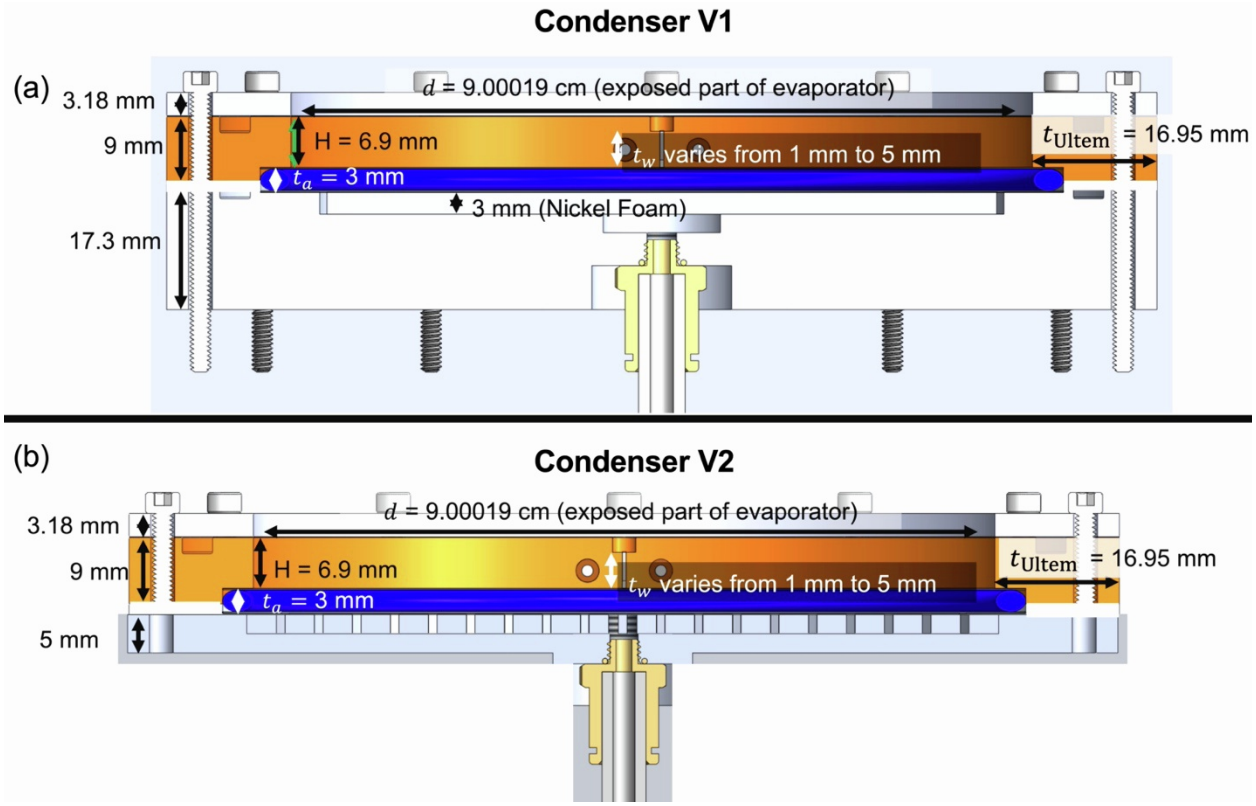

Figure S12. A SolidWorks drawing of the cross section of the device. (a) Dimensions of Condenser V1. (b) Dimensions of Condenser V2.

Consider the heat and mass transfer at steady state condition (Figure S11), the evaporator absorbs heat from the sunlight $Q_{\text{ab}} = \tau_{\text{f}}\alpha_{\text{a}}\, q_{\text{solar}}\, A_0$, where $q_{\text{solar}} = 1000$ W m^{-2}, $\tau_{\text{f}} = 0.9$ is the transmittance of the ETFE film, and $\alpha_a = 0.9$ is the absorptance of the evaporator membrane, and absorber area $A_0 = {}^{\pi\, d^2}/_4 \approx 0.0064$ m^2 with diameter $d \approx 9$ cm. Evaporation occurs on the membrane, which removes heat $\dot{m}\, h_{\text{fg}}$ from the evaporator membrane, where $\dot{m}$ is the mass flow rate of vapor production (kg/s) and h_{fg} is the latent heat of vaporization. In addition, the evaporator loses heat through the top surface Q_{top}, through the side Ultem Q_{side}, and through the air gap to the condenser Q_{air}. The sensible heat loss of the discharged salt water is neglected by assuming effective heat recycling due to the counter-flow heat exchanger. Heat conduction through the O-ring from the evaporator to the condenser is neglected due to its minimal contact area with the membranes. The vapor condenses on the condenser membrane, which releases heat $\dot{m}\, h_{\text{fg}}$ on the condenser membrane. The condenser membrane also receives heat from the evaporator through heat conduction across the air gap Q_{air}, and rejects heat to the ambient via the aluminum Q_{bottom}.

An equivalent thermal resistance network is illustrated in Figure S11b. Balancing the heat gain and heat loss at the evaporator membrane (T_{e}) and condenser membrane (T_{c}) requires

$$Q_{\text{ab}} - \frac{T_{\text{e}} - T_{\text{amb}}}{R_{\text{top}}} - \frac{T_{\text{e}} - T_{\text{amb}}}{R_{\text{side}}} - \frac{T_{\text{e}} - T_{\text{c}}}{R_{\text{a}}} - \dot{m}h_{\text{fg}} = 0 \tag{S1}$$

$$\dot{m}h_{\text{fg}} + \frac{T_{\text{e}} - T_{\text{c}}}{R_{\text{a}}} - \frac{T_{\text{c}} - T_{\text{amb}}}{R_{\text{bottom}}} = 0 \tag{S2}$$

In equations (1-2), T_e, T_c, and T_amb are temperatures of the evaporation interface (or the evaporator membrane), the condensation interface (or the condenser membrane), and the ambient. R_top, R_side, R_a and R_bottom are the total thermal resistances for Q_top, Q_side, Q_air and Q_bottom, detailed below. Furthermore, vapor transport between the evaporator and the condenser is governed by Fick's diffusion law,

$$\dot{m} = A_0 D\left[\frac{c_\mathrm{sat}(T_\mathrm{e}) - c_\mathrm{sat}(T_\mathrm{c})}{t_\mathrm{a}}\right] \tag{S3}$$

where D is the diffusivity of water vapor in air, $c_\mathrm{sat}(\mathrm{T})$ is the saturation vapor mass concentration as a function of temperature as:

$$c_\mathrm{sat}(T) = \frac{PM}{R\,T},$$

where P is the saturation pressure of water vapor and can be calculated using the Antoine equation:

$$\log_{10}P = 8.07131 - \frac{1730.63}{233.426 + T}.$$

Equations (S1)-(S3) have three unknowns: T_e the evaporator membrane temperature, T_c the condenser membrane temperature, and $\dot{m}$ the mass flow rate which is equal to the distillate production rate at steady state. These unknowns can be numerically solved. The resulting solar-to-water efficiency is then expressed as

$$\eta = \frac{\dot{m}\,h_\mathrm{fg}}{q_\mathrm{solar}\,A_0} \tag{S4}$$

The thermal resistances in equations (1) and (2) are:

$$R_\mathrm{top} = \frac{1}{A_0}\left(\frac{t_\mathrm{w}}{k_\mathrm{w}} + \frac{t_\mathrm{ETFE}}{k_\mathrm{ETFE}} + \frac{1}{h_\mathrm{top}}\right) \tag{S5}$$

where t_w and t_ETFE are the thicknesses of the water layer in the evaporator (1 mm) and the ETFE film (0.005 inch), respectively. k_w and k_ETFE are the thermal conductivity of water and ETFE, respectively. h_top is the natural air convection heat transfer coefficient on top of the ETFE film.

R_top represents the total thermal resistance of heat conduction across the water, ETFE, and natural air convection into the ambient.

$$R_\mathrm{side} = \frac{1}{A_\mathrm{side}}\left(\frac{t_\mathrm{Ultem}}{k_\mathrm{Ultem}} + \frac{1}{h_\mathrm{side}}\right) \tag{S6}$$

where t_Ultem is the thickness of the Ultem fixture, k_{Ultem} is the thermal conductivity of the Ultem, and h_{side} is the heat transfer coefficient of air on the external surface of Ultem. $A_\mathrm{side} \approx t_\mathrm{Ultem}\pi d$ is the Ultem sidewall area. Here we used one-dimensional conduction to approximate the heat conduction in Ultem when t_{Ultem} is much smaller than the water layer. The actual heat conduction in Ultem of the device that we fabricated is more complex due to its geometry, which is numerically simulated in COMSOL (see Section B). In a scaled-up device, heat loss through the side is negligible compared to heat loss from the top because $A_{side} \ll A_0$.

$$R_a = \frac{1}{A_0}\left(\frac{t_\mathrm{a}}{k_\mathrm{a}}\right) \tag{S7}$$

where t_a is the thickness of the air gap between the evaporator membrane and the condenser membrane, k_a is the thermal conductivity of air.

$$R_\mathrm{bottom} = \frac{1}{A_0}\left(\frac{t_\mathrm{comp}}{k_\mathrm{comp}} + \frac{t_\mathrm{Al}}{k_\mathrm{Al}} + \frac{1}{h_\mathrm{bottom}}\right) \tag{S8}$$

where t_comp and t_Al are the thicknesses of the composite and the aluminum condenser; k_comp and k_Al are the thermal conductivity of composite and aluminum, respectively; h_bottom is the natural air convection heat transfer coefficient on bottom of the aluminum condenser.

B. Model validation via 7 day passive experiment

To validate the model framework, we numerically solved equations (1)-(3) in MATLAB using thermophysical properties listed in **Table S1**. The ambient temperature is 20 °C. The natural air convection heat transfer coefficient typically ranges from 5-25 W m^{-2} K^{-1}. Based on correlations (equation 9) for air on top of a hot flat surface for low Rayleigh numbers, h = 7 W m^{-2} K^{-1}.[1] Considering minor air flow due to air-conditioning in the lab environment, we used $h_{top} = h_{bottom}$ = 10 W m^{-2} K^{-1} in the model. The mass diffusivity D of water vapor in air is 2.773×10^{-5} m^2/s (see notes S.3) based on Chapman-Enskog theory.[2-5]

$$\overline{\mathrm{Nu}}_{L^*} = \frac{0.560\,\mathrm{Ra}_{L^*}^{1/4}}{[1+(0.492/\mathrm{Pr})^{9/16}]^{4/9}}$$

$$\overline{\mathrm{Nu}}_{\mathrm{corrected}} = \frac{1.4}{\ln\left(1+\frac{1.4}{\overline{\mathrm{Nu}}_{L^*}}\right)} \qquad \text{(S9)}$$

L* = A/P where A is the area of a horizontal plate and P is the perimeter.

Since the actual geometry of the Ultem is complex and the heat conduction cannot be approximated using a 1D model, we estimated R_{side} using COMSOL. On the Ultem, the area contacting water is set to be T_e, and we applied a natural air convection heat transfer coefficient of 10 $Wm^{-2}K^{-1}$ on the Ultem surface exposed to the ambient. Q_{side} was obtained by integrating the heat flux over the exposed surface area. R_{side} was estimated as

$$R_{side} = \frac{T_e - T_{amb}}{Q_{side}} \qquad \text{(S10)}$$

In COMSOL, by setting T_e=50 °C, T_{amb}=20 °C, we obtain Q_{side} = 0.907 W. Therefore, R_{side} = 33.3 K/W. The temperature distribution in the Ultem is shown in Figure S13. Since thermal resistance is not a function of the applied temperature difference, R_{side} is constant for any T_e.

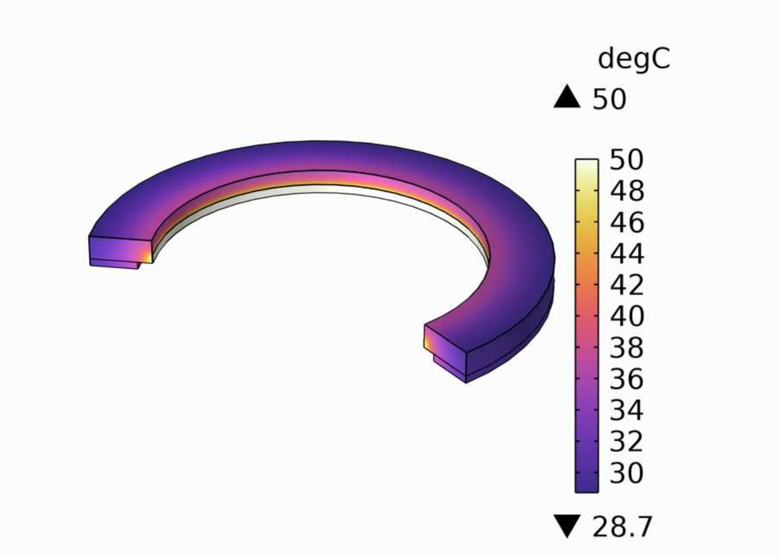

Figure S13. The temperature distribution in the Ultem fixture. Only part of the Ultem is shown to illustrate the cross-sectional temperature.

Based on these inputs we solved equations (1)-(3) numerically and obtained that
T_c = 51.65 °C, T_e=54.67 °C, and a solar-to-water efficiency of 28.87%, which are very close to the experimentally observed values.

Table S1. Thermophysical properties and thicknesses of the materials used in the model

	Thermal conductivity, k (W/m. K)	Thickness, t (mm)
Ultem (PEI)	0.22	--
ETFE	0.238	0.127
Aluminum	238	14
Water	0.615	Varies from 1 – 5
Aluminum	238	5
Air	0.0277	--
composite (80% water, 20% nickel)	18.62	3
Nickel*	90.7	--

* Properties of nickel is not used in the model, but rather in calculating the properties of the composite layer

Supplemental Note S.3: Diffusivity coefficient

To understand the theoretical maximum mass transport of water through air from the evaporator to the condenser, we use Fick's law of diffusion,

$$m'' = D_{H_2O,air}\,\frac{c(T_e) - c(T_c)}{z}, \tag{S11}$$

where $c(T_e)$and $c(T_c)$are the saturated vapor concentrations at the evaporator (with temperature $T_{evaporator}$) and the condenser (with temperature $T_{condenser}$). The length, z is the distance between the evaporator and the condenser. For this model, z = 3 mm. In this model, we considered the temperature-dependent mass diffusivity D_{AB} of binary species, as per Chapman-Enskog theory[1–4],

$$D_{AB} = \frac{1.8583\ \times 10^{-7}\, T^{\frac{3}{2}}}{p{\sigma_{AB}}^2\Omega_D}\sqrt{\frac{1}{M_A}+\frac{1}{M_B}}, \tag{S12}$$

where the value, $1.8583\ \times 10^{-7}$ is an empirical coefficient, p is the ambient pressure and σ_{AB} is the average collision diameter. The air temperature, T is computed by taking the average of evaporator and condenser temperatures. Ω_D is the collision integral for diffusivity. M_A and M_B are the molar mass of the two species: water and air.

We compute the diffusivity, D_{AB} for the diffusion of H_2O in air at 318.5 K and 1 atm. Let air be species A and H_2O be species B. ε_A is the potential well depth for species A and ε_B is the potential well depth for species B. The potential well depth is a measure of how strongly two particles attract each other. ε_{AB} is a measure of how strongly species A is attracted to species B. k_B is the Boltzmann constant.

For the given conditions, using table 11.2 from Lienhard IV et. al. calculated from mass diffusion data we determine the Lennard-Jones constants.[5,6]

$$\sigma_A = 3.711\ \text{Å} \ \text{ and } \sigma_B = 2.655\ \text{Å},$$

$$\frac{\varepsilon_A}{k_B} = 78.6\,K \text{ and } \frac{\varepsilon_B}{k_B} = 363\,K.$$

From these constants, we can calculate the following values for the air-water mixture.

$$\sigma_{AB} = \frac{\sigma_A + \sigma_B}{2} = 3.183\ \text{Å},$$

$$\frac{\varepsilon_{AB}}{k_B} = \sqrt{\left(\frac{\varepsilon_A}{k_B}\right)\left(\frac{\varepsilon_B}{k_B}\right)} = 169\,K,$$

$$\frac{k_B T}{\varepsilon_{AB}} = 1.8856.$$

Hence, $\frac{\varepsilon_{AB}}{k_B} = 168.9136\,K$ and $\Omega_D = 1.0972$ from table 11.3 from Lienhard IV et. al.[5] Then,

$$D_{AB} = \frac{1.8583 \times 10^{-7}\, T^{\frac{3}{2}}}{(1)(3.183)^2(1.0972)}\sqrt{\frac{1}{28.96}+\frac{1}{18.02}} = 2.7773 \times 10^{-5}\ {m^2}/{s}$$

An empirical correlation for the water air mixture can also be used. [5]

$$D_{H_2O,air} = \frac{1.87 \times 10^{-10}\, T^{2.072}}{p} \text{ for } 282\,K \le T \le 450\,K. \quad \text{(S13)}$$

Using T = 318.5 K for this empirical correlation, we get: $D_{H_2O,air} = 2.873 \times 10^{-5}$ m^2/s. The prediction is within 4% of the computed value.

Supplemental Note S.4: ion concentration of the distillate

We monitored ion concentrations of Boron, Barium, Calcium, Magnesium, Sodium and Strontium in the distillate using ICP. We found that all ion concentrations of these elements in the distillate were well below the WHO health guidelines and below the taste thresholds as well.[7]

Table S2. ICP data

	B (mg/L)	Ba (mg/L)	Ca (mg/L)	Mg (mg/L)	Na (mg/L)	Sr (mg/L)
WHO guideline	2.4	1.3	100-300 (Taste threshold)	<100 (Taste threshold)	200	N/A
Distillate (7 day desalination using passive gravity driven flow)	--	--	0.23	0.74	0.15	0
Distillate (7 day desalination using syringe pump)	0.11	0	3.21	1.47	0.32	0.06
Distillate (25 hour desalination using passive gravity driven flow)	0.02	--	1.26	0.79	0.56	0.01

Supplemental References

1. Fernandez de la Mora, J., and Fernandez-Feria, R. (1987). Two-fluid Chapman–Enskog theory for binary gas mixtures. Physics of Fluids *30*, 2063. 10.1063/1.866141.
2. Fuller, E.N., Schettler, P.D., and Giddings, J.Calvin. (1966). NEW METHOD FOR PREDICTION OF BINARY GAS-PHASE DIFFUSION COEFFICIENTS. Ind Eng Chem *58*, 18–27. 10.1021/ie50677a007.
3. Chapman, S., and Cowling, T.G. (1990). The Mathematical Theory of Non-uniform Gases: An Account of the Kinetic Theory of Viscosity, Thermal Conduction and Diffusion in Gases 3rd ed. (Cambridge University Press).
4. Chapman, S., and Cowling, T.G. (1939). Growth of Kinetic Theory. Nature, 993–995.
5. Lienhard IV, J.L.V.J. (2019). A Heat Transfer Textbook Fifth. (Dover Publications).
6. Smit, B. (1992). Phase diagrams of Lennard-Jones fluids. J Chem Phys *96*, 8639–8640. 10.1063/1.462271.
7. Guidelines for drinking-water quality: Fourth edition incorporating the first and second addenda (2022). 4th ed. (World Health Organization).